

La₃Li₃W₂O₁₂: Ionic Diffusion in a Perovskite with Lithium on both A- and B-Sites

Alma B. Santibáñez-Mendieta,[†] Christophe Didier,[†] Kenneth K. Inglis,[†] Alex J. Corkett,[†] Michael J. Pitcher,[†] Marco Zanella,[†] J. Felix Shin,[†] Luke M. Daniels,[†] Aydar Rakhmatullin,[‡] Ming Li,[§] Matthew S. Dyer,[†] John B. Claridge,[†] Frédéric Blanc,^{*,†,||} and Matthew J. Rosseinsky^{*,†}

[†]Department of Chemistry, University of Liverpool, Crown Street, Liverpool L69 7ZD, United Kingdom

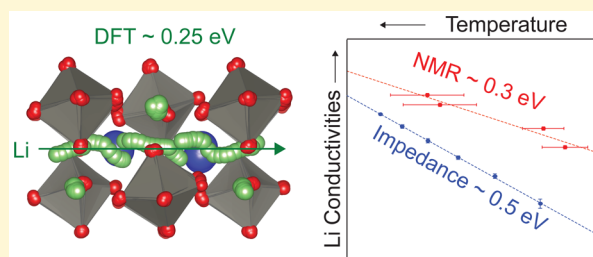
[‡]CEMHTI-CNRS UPR3079, Conditions Extrêmes et Matériaux: Haute Température et Irradiation, Av. de la Recherche Scientifique, 45071 Orléans cedex 2, France

[§]Faculty of Engineering, University of Nottingham, University Park, Nottingham NG7 2RD, United Kingdom

^{||}Stephenson Institute for Renewable Energy, University of Liverpool, Crown Street, Liverpool L69 7ZD, United Kingdom

Supporting Information

ABSTRACT: The structure and Li⁺ ion dynamics of a new class of ABO₃ perovskite with Li on both the A- and B-sites are described. La₃Li₃W₂O₁₂ is synthesized by solid state reaction at 900 °C and shown by powder X-ray diffraction to adopt the structure of a monoclinic double perovskite (A₂)BB'O₆, (La_{1.5}Li_{0.5})WLiO₆, with rock salt order of W⁶⁺ and Li⁺ on the B-site. High resolution powder neutron diffraction locates A-site Li in a distorted tetrahedron displaced from the conventional perovskite A-site, which differs considerably from the sites occupied by Li in the well studied La_{2/3-x}Li_{3x}TiO₃ family. This is confirmed by the observation of a lower coordinated Li⁺ ion in the ⁶Li magic angle spinning nuclear magnetic resonance (NMR) spectra, in addition to the B-site LiO₆, and supported computationally by density functional theory (DFT), which also suggests local order of A-site La³⁺ and Li⁺. DFT shows that the vacancies necessary for transport can arise from Frenkel or La excess defects, with an energetic cost of ~0.4 eV/vacancy in both cases. *Ab initio* molecular dynamics establishes that the Li⁺ ion dynamics occur by a pathway involving a series of multiple localized Li hops between two neighboring A-sites with an overall energy barrier of ~0.25 eV, with additional possible pathways involving Li exchange between the A- and B-sites. A similar activation energy for Li⁺ ion mobility (~0.3 eV) was obtained from variable temperature ⁶Li and ⁷Li line narrowing and relaxometry NMR experiments, suggesting that the barrier to Li hopping between sites in La₃Li₃W₂O₁₂ is comparable to the best oxide Li⁺ ion conductors. AC impedance-derived conductivities confirm that Li⁺ ions are mobile but that the long-range Li⁺ diffusion has a higher barrier (~0.5 eV) which may be associated with blocking of transport by A-site La³⁺ ions.



1. INTRODUCTION

Replacing liquid electrolytes with solid ceramics or polymers in next-generation battery technologies is of growing interest due to the major impact that will result from the increase in lifetime and safety, higher power outputs and higher energy densities expected in energy storage appliances.¹ Lithium has become the element of choice in most battery designs because of the high mobilities arising from its small ionic radius. Hence, a major goal of the field is to synthesize lithium-based ceramics with ionic conductivities that equal or surpass current liquid electrolytes.

The fastest crystalline inorganic Li⁺ ion conductors reported to date are sulfides such as Li₁₀GeP₂S₁₂,² with a room temperature conductivity of 0.012 S/cm, and the related Li₁₁Si₂PS₁₂.³ The high conductivities arise from the presence of many potential sites for the Li cations that provide low energy pathways through these structures. Despite their high Li⁺ conductivities, the practical applications of these compounds

are limited by their tendency to decompose under ambient conditions, producing H₂S when in contact with moisture, which necessitates handling in inert atmospheres.⁴ Oxides are generally more chemically stable, and the doped garnet Li₇La₃Zr₂O₁₂ and the ABO₃ perovskite La_{2/3-x}Li_{3x}TiO₃ (LLTO; A = La, Li, B = Ti) systems have respectable conductivities in the region of 10⁻³ S/cm which arise from motion of the Li occupying the A-site between the O₁₂ anion cages that define these sites.^{5,6} However, bulk ionic conductivity in LLTO may be limited by the presence of La³⁺ rich and La³⁺ poor A-site layers within the crystal structure, arising from the 2D diffusion of Li⁺ ions at lower temperature and 3D diffusion at higher temperature.⁷⁻⁹ In addition, the grain boundary conductivity is 1 order of magnitude lower than

Received: August 9, 2016

Revised: September 28, 2016

Published: September 30, 2016

the bulk conductivity, reducing the total conductivity of LLTO ceramics,⁵ and the reduction of Ti^{4+} to Ti^{3+} at the anode side of a cell leads to electronic conductivity and limits the practical use of LLTO as a Li^+ ion electrolyte.¹⁰ One solution to the problem of high electronic contribution to the conductivity is to replace Ti^{4+} with stable $4d^0$ or $5d^0$ cations such as Nb^{5+} and W^{6+} : this has inspired the synthesis of several analogues of LLTO, including the perovskites $\text{La}_{1/3-x}\text{Li}_{3x}\text{NbO}_3$ ($x < 0.1$),^{11,12} $\text{La}_{1/3-x}\text{Li}_{3x}\text{TaO}_3$ ^{13–16} ($x < 0.17$) and the double perovskite $\text{La}_{4-x}\text{Li}_x\text{Mg}_3\text{W}_3\text{O}_{18}$ ¹⁷ ($x < 0.05$) in which Li^+ ions have been introduced to the partially vacant A-site by aliovalent substitution. The activation energies for Li conduction in such compounds are thought to be affected by the size of the windows between A-sites (dependent on the size of the B cation and directly affected by structural distortion), and also by the degree of covalency in the B–O bond,¹⁷ as implied by the complex variation of ionic conductivity with composition and lattice parameter in LLTO-derived systems such as $(\text{La}_{1-x}\text{Nd}_x)_{0.56}\text{Li}_{0.33}\text{Ti}_{1-x}\text{O}_3$ and $\text{La}_{0.56}\text{Li}_{0.33}\text{M}_x\text{Ti}_{1-x}\text{O}_3$ ($\text{M} = \text{Zr}^{4+}, \text{Hf}^{4+}$),^{18,19} and related double perovskite systems such as $\text{LiSr}_{2-x}\text{Ti}_{2-2x}\text{Ta}_{1+2x}\text{O}_9$,^{20,21} whose octahedral BO_6 networks are not distorted substantially away from those of LLTO. Despite the suppression of electronic conductivity in these compounds, the resulting ionic conductivities are lower than those seen in LLTO.

One approach to increasing ionic conductivity is to increase the number of potential migration pathways for Li^+ ions. The perovskite A-site is not the only position that can accommodate Li^+ ions; there are many known double perovskites in which the B-site is occupied by an ordered array of Li^+ ions and a tetra-, penta- or hexavalent cation, such as $\text{LaLi}_{1/3}\text{Ti}_{2/3}\text{O}_3$ (which exists in the same La_2O_3 – Li_2O – TiO_2 phase diagram as LLTO^{22,23}), $\text{SrLi}_{0.4}\text{W}_{0.6}\text{O}_3$ ²⁴ and the series La_2LiMO_6 ($\text{M} = \text{V}, \text{Nb}, \text{Ta}, \text{Mo}, \text{Re}, \text{Ru}, \text{Os}, \text{Ir}$ and Sb),^{25–27} as well as perovskites with combinations of Li, Nb and W on the B-site.^{28,29} Such compounds retain the advantage of negligible electronic conductivity, but are rarely considered as ionic conductors due to the lack of an obvious conduction pathway between Li sites, and the paucity of examples of stable B-site vacancies in perovskites. However, consideration of intersite distances in the perovskite structure suggests that their structural features may offer a way of enhancing the ionic conductivities of the A-site Li perovskites: assuming an undistorted double perovskite with 1:1 rock-salt ordering on the B-sites, the distance between adjacent B- and A-sites ($=\sqrt{3}/2a_p$) is considerably shorter than that between two B-site Li^+ ions ($\sqrt{2}a_p$) and shorter than that between two adjacent A-sites (a_p). Hence, it is plausible that a perovskite with Li on both the A- and B-sites would exhibit exchange between the sites, offering the potential to enhance ionic conductivity considerably by opening up multiple pathways to Li^+ ion motion throughout the crystal structure. To date, there have been no reports of such a compound, despite the prevalence of both individual classes of structure.

Here we present the synthesis of such a material with composition $\text{La}_3\text{Li}_3\text{W}_2\text{O}_{12}$, in which one-quarter of the A-sites and one-half of the B-sites are occupied by Li^+ ions. The composition, crystal structure and Li^+ ion dynamics of $\text{La}_3\text{Li}_3\text{W}_2\text{O}_{12}$ are obtained and discussed through a combination of experimental and computational techniques. X-ray and neutron diffraction, electron microscopy and solid-state ^6Li and ^{17}O nuclear magnetic resonance (NMR) spectroscopy experiments combined with density functional theory (DFT)

calculations are used to provide understanding of the crystal structure and the local Li environments. Additionally, insights into the Li^+ ion dynamics are obtained by acquiring variable temperature ^6Li and ^7Li solid-state NMR data and measuring the Li^+ ion conductivities by AC impedance spectroscopy (ACIS), and supported by computational modeling using *ab initio* molecular dynamics (AIMD) simulations.

2. MATERIALS AND METHODS

2.1. Synthesis and Chemical Analysis. $\text{La}_3\text{Li}_3\text{W}_2\text{O}_{12}$. Powder samples of $\text{La}_3\text{Li}_3\text{W}_2\text{O}_{12}$ were prepared by a conventional high-temperature ceramic method. A stoichiometric mixture of La_2O_3 (99.99% Sigma-Aldrich, dried at 950 °C for 12 h), Li_2CO_3 (>99% Sigma-Aldrich, dried at 250 °C for 12 h) and WO_3 (99.9% Fluka, dried at 250 °C for 12 h) was ball-milled in ethanol; the resulting slurry was then dried, homogenized with a pestle and mortar (thus reversing any possible separation of the reactants by sedimentation upon drying), and a portion of the reaction mixture was pelletized. The pellet was loaded into an alumina crucible lined with gold foil, buried in sacrificial powder of the same composition (i.e., the remainder of the reaction mixture), and subjected to a two-step firing process: first, the sample was heated in air to 900 °C at a rate of 5 °C/min and held for 5 h before cooling back to room temperature at 5 °C/min. PXRD shows that this step produces the targeted perovskite phase, but its crystallinity is relatively low, as indicated by broad Bragg peaks. To improve the crystallinity and homogeneity, the sample was reground by hand, repelletized, loaded into a gold-foil-lined alumina crucible and packed under the same sacrificial powder, and then subjected to a second annealing in air at 900 °C for 60 h (heated and cooled at a rate of 5 °C/min). This was found to produce highly crystalline single-phase samples of $\text{La}_3\text{Li}_3\text{W}_2\text{O}_{12}$.

$\text{La}_{2/3}\text{Li}_{0.4}\text{W}_{0.6}\text{O}_3$. For the initial synthesis of samples purified with washing, a mixture of La_2O_3 (99.99% Sigma-Aldrich, dried at 900 °C overnight), Li_2CO_3 (>99% Sigma-Aldrich, dried at 250 °C overnight) and WO_3 (99.9% Fluka, dried at 250 °C overnight) for target composition $\text{La}_{2/3}\text{Li}_{1.34}\text{W}_{0.6}\text{O}_{3.3}$ was ball-milled overnight, and pelletized after homogenization in a mortar. A gold foil was placed between the alumina crucible and the pellet itself was covered in sacrificial powder of the same composition. The sample was then annealed twice in ambient air at 900 °C for 5 h and once for 45 h with intermediate hand-grinding and pelletizing, using the same sacrificial powder. The PXRD pattern of the resulting powder shows a mixture of the perovskite phase subsequently identified as $\text{La}_3\text{Li}_3\text{W}_2\text{O}_{12}$ and Li_4WO_5 impurity (PDF no. 00-021-0530). This impurity can be removed by sonicating the powder in dilute nitric acid (roughly 1 g of powder per 60 mL of a 25 mmol/L solution of HNO_3 in water) for 5 min. The powder is then filtered, washed several times with distilled water and left to dry at 100 °C.

Isotopically Enriched Samples for Neutron Diffraction and NMR. As ^6Li has a very large absorption cross section, neutron diffraction experiments were performed on a ^7Li enriched $\text{La}_3\text{Li}_3\text{W}_2\text{O}_{12}$ prepared using the same synthesis pathway and using ^7Li enriched Li_2CO_3 (99% ^7Li , Sigma-Aldrich, predried at 200 °C) as the lithium precursor. Because of the low NMR receptivity of ^6Li ,³⁰ ^6Li enriched $\text{La}_3\text{Li}_3\text{W}_2\text{O}_{12}$ ($\text{La}_3^6\text{Li}_3\text{W}_2\text{O}_{12}$) was also synthesized by using $^6\text{Li}_2\text{CO}_3$ (99.9% ^6Li , Sigma-Aldrich, predried at 200 °C). ^{17}O enriched $\text{La}_3\text{Li}_3\text{W}_2\text{O}_{12}$ ($\text{La}_3\text{Li}_3\text{W}_2^{17}\text{O}_{12}$) was prepared by a gas–solid exchange reaction with ^{17}O enriched O_2 gas (60% ^{17}O , Sigma-Aldrich, used as received).³¹ A sealed quartz tube containing $\text{La}_3\text{Li}_3\text{W}_2\text{O}_{12}$ in a ^{17}O enriched O_2 gas atmosphere was heated at 5 °C/min to 600 °C and held for 12 h. The sample was then cooled to room temperature at a rate of 5 °C/min.

Transmission Electron Microscopy Energy Dispersive X-ray Spectroscopy. TEM-EDX was performed in a JEOL 2000FX equipped with an EDAX spectrometer. A small amount of powder from each sample was dispersed in a small quantity of ethanol and deposited on a copper TEM grid. Ten particles were chosen at random and analyzed to determine the powder composition, and correction factors obtained from suitable reference compounds were applied to the raw data.

Compositional Analyses. Inductively coupled plasma optical emission spectrometry (ICP-OES) was used for compositional analysis. A solution of $\text{La}_3\text{Li}_3\text{W}_2\text{O}_{12}$ in H_2O was prepared by dissolving the solid (approximately 60 mg) in 1.1 M of HNO_3 (7 mL) and 0.9 M of H_2O_2 (3 mL) making up to 100 mL with deionized H_2O . Metal contents were corrected for interference by comparing separate and combined metal solutions of known concentrations (25 mg/L). Experiments were performed on a Ciroso (Spectro) radial view instrument.

Dilatometry Measurements. The measurements for a 6 mm diameter pellet of $\text{La}_3\text{Li}_3\text{W}_2\text{O}_{12}$ were performed on a DIL 402C (Netzsch) push-rod dilatometer under ambient air. The pellet was covered in platinum foil to avoid contamination of the alumina spacers. The sample was heated to 700 °C at a rate of 5 °C/min followed by a slower heating rate of 2 °C/min up to 860 °C, followed by a holding time of 24 h at 860 °C before a cooling step at a rate of 5 °C/min down to 50 °C.

2.2. Diffraction Experiments. Powder X-ray diffraction (PXRD) data for initial phase identification and indexing were collected in Bragg–Brentano mode on a Panalytical X'Pert Pro diffractometer using monochromated $\text{Co K}_{\alpha 1}$ radiation ($\lambda = 1.7890$ Å). High resolution synchrotron PXRD data (SXRD) were collected at room temperature at beamline I11 (Diamond, UK) with an incident wavelength of 0.826 185(5) Å, using five multianalyzer crystal detectors with the sample contained in a spinning borosilicate capillary. Rietveld refinements against SXRD data were carried out using Topas Academic version 5,³² against data in the $5 \leq 2\theta \leq 90^\circ$ range and using Chebyshev background (18 terms) and Pearson-VII peak profile functions.

High resolution time-of-flight powder neutron diffraction data (PND) were collected at HRPD (ISIS, UK) at room temperature and 5 K from a sample enriched with ^7Li to minimize absorption by ^6Li . Room temperature data were collected from the high resolution back scattering detector bank ($2\theta = 168^\circ$) using a pulse window of 30–130 ms, corresponding to a d -spacing range of $0.6 < d < 2.6$ Å. For the data collection at 5 K, the pulse window was adjusted to 10–110 ms to allow a d -spacing range $0.2 < d < 2.2$ Å. In both cases, long data acquisition times were used to ensure adequate counting statistics at the smallest d -spacings. All data were corrected for absorption prior to Rietveld analysis. Rietveld refinements against PND data were carried out using GSAS.^{33,34}

2.3. Computational Details. All calculations were performed using plane-wave based periodic density functional theory (DFT) with the PBE functional.³⁵ VASP³⁶ was used for the bulk of calculations, with the projector augmented wave method³⁷ used to treat core electrons. An energy cutoff of 600 eV was imposed, with k -point grids corresponding to a $4 \times 4 \times 3$ grid in the 20 atom experimental cell. Unit cell parameters and atomic positions were optimized until forces on atoms reached 0.01 eV/Å. The relative energies of structures calculated using a larger k -point grid ($7 \times 7 \times 5$) and tighter force threshold (0.001 eV/Å) differed by less than 0.01 eV/formula unit (FU). Normal mode calculations were carried out at the Γ point using finite differences and the harmonic approximation. Partial occupancies of the electronic states were set using a Gaussian of width 0.01 eV.

Ab initio molecular dynamics (AIMD) calculations were performed using the NVT ensemble, with the cell fixed to the DFT optimized cell parameters of the starting structure. A 1 ps equilibration run was performed with the temperature rescaled at each step to the target temperature. For subsequent production runs, a Nosé thermostat was used, and the charge density recalculated every 1 ps. At high temperatures, a broader 0.1 eV wide Gaussian was used to aid convergence of the electronic states.

Nudged Elastic Band (NEB) calculations were performed with initially six, and then 12 images along each path. The position of one W atom was fixed across the trajectory to prevent translational drift occurring during structural optimization. Cell parameters and atomic positions were optimized until forces on atoms reached 0.01 eV/Å.

NMR parameters were calculated using GIPAW^{38,39} as implemented in CASTEP⁴⁰ on the three most stable calculated configurations: C1, C2 and C3 (see below). Before NMR parameters

were calculated, structures were reoptimized starting from those obtained using VASP, with a higher cutoff energy of 700 eV, and a force threshold of 0.001 eV/Å. The calculated isotropic magnetic shieldings (σ_{iso}) were converted to the isotropic chemical shifts (δ_{iso}) to allow comparison with the experimental values using the following expression $\delta_{\text{iso}} = 223.7 - 0.888\sigma_{\text{iso}}$ for ^{17}O shifts⁴¹ and $\delta_{\text{iso}} = 86.9 - 0.961\sigma_{\text{iso}}$ for ^6Li shifts (see SI). The quadrupole coupling constants are obtained as $C_Q = eQV_{zz}/h$ and the asymmetry parameter as $\eta_Q = (V_{xx} - V_{yy})/V_{zz}$, where an ordering $|V_{zz}| \geq |V_{yy}| \geq |V_{xx}|$ of the principal components of the traceless electric field gradient tensor is assumed.

2.4. Nuclear Magnetic Resonance Experimental Details. ^6Li magic angle spinning (MAS) solid-state NMR experiments were carried out on a 9.4 T Bruker Avance III HD spectrometer equipped with a Bruker 4 mm HXY MAS probe (in double resonance mode) tuned to X = ^6Li at a Larmor frequency $\nu_0(^6\text{Li}) = 58.88$ MHz and on a 20 T Bruker Avance II spectrometer with a Bruker 4 mm HX MAS probe tuned to ^6Li at $\nu_0(^6\text{Li}) = 125.11$ MHz. ^6Li spectra were obtained with a $\pi/2$ pulse length of 3 μs at a radio frequency (rf) amplitude of $\nu_1(^6\text{Li}) = 83$ kHz at a MAS rate of 10 kHz. Additional ^6Li MAS NMR spectra were recorded on the same 9.4 T NMR spectrometer with a Bruker 1.3 mm HXY MAS probe at with a $\pi/2$ pulse length of 3 μs at a rf amplitude of $\nu_1(^6\text{Li}) = 83$ kHz at a MAS rate of 60 kHz.

^{17}O rotor synchronized Hahn echo and two-dimensional (2D) z -filtered multiple-quantum MAS (MQMAS)^{42–44} experiments were carried out on a 9.4 T Bruker Avance III HD spectrometer with a Bruker 4 mm HXY MAS probe (in double resonance mode) tuned to ^{17}O at $\nu_0(^{17}\text{O}) = 54.2$ MHz and at a MAS rate of 13 kHz, and on a 20 T Bruker Avance II spectrometer with a Bruker 3.2 mm HXY MAS probe (in double resonance mode) tuned to ^{17}O at $\nu_0(^{17}\text{O}) = 115.3$ MHz and at a MAS rate of 20 kHz. ^{17}O spectra were obtained with $\pi/2$ pulse lengths of 1 and 1.2 μs at a rf amplitude of $\nu_1(^{17}\text{O}) = 83$ and 70 kHz at 20 and 9.4 T, respectively. Excitation and reconversion pulses in the 2D ^{17}O 3QMAS NMR experiments were performed at rf amplitude of $\nu_1(^{17}\text{O}) \approx 83$ kHz, whereas the selective $\pi/2$ was obtained at 13 kHz.

All variable temperature ^6Li and ^7Li solid-state NMR experiments were obtained under static conditions at 9.4 T and with $\nu_0(^6\text{Li}) = 58.88$ MHz and $\nu_0(^7\text{Li}) = 155.51$ MHz, respectively. Below 650 K, experiments were conducted on a 9.4 T Bruker Avance III HD spectrometer with a Bruker 4 mm HX high temperature MAS probe (between 294 and 650 K) and with a Bruker 4 mm HXY MAS probe (in double resonance mode below 294 K) using standard 4 mm ZrO₂ rotors and caps. Above 650 K, experiments were carried out on a 9.4 T Bruker Avance spectrometer using a single channel high temperature static NMR probe with a homemade CO₂ laser ($\lambda = 10.6$ μm , 250 W) heating system developed in Orléans (CEMHTI–CNRS, France).^{45,46} The sample was placed in a BN crucible and inserted into the rf coil of the high temperature NMR probe. The sample is heated up by two lasers, passing axially through the NMR probe, with the sample temperature controlled by the laser power output. A flow of N₂ is used to cool the rf coil and a flow of Ar gas to prevent oxidation of the BN crucible at high temperature. ^6Li spectra were obtained with a $\pi/2$ pulse of 3 μs at an rf amplitude of $\nu_1(^6\text{Li}) = 83$ kHz below 650 K and with a $\pi/2$ pulse of 52.5 μs at an rf amplitude of $\nu_1(^6\text{Li}) = 4.7$ kHz above 650 K. ^7Li spectra were obtained with a $\pi/2$ pulse of 2 μs at an rf amplitude of $\nu_1(^7\text{Li}) = 62.5$ kHz below 650 K and with a $\pi/2$ pulse of 8 μs at an rf amplitude of $\nu_1(^7\text{Li}) = 15$ kHz above 650 K. Spin–lattice relaxation times in the laboratory frame (T_1) were obtained using a saturation recovery pulse sequence and the data were fitted to a stretched exponential of the form $1 - \exp[-(\tau/T_1)^\alpha]$, where τ are variable delays and α is the stretch exponential coefficient (between 0.85 and 1). ^7Li spin–lattice relaxation times in the rotating frame ($T_{1\rho}$) were obtained with a spin-lock pulse sequence at frequencies of $\nu_1(^7\text{Li}) = 8$ and 14 kHz. $T_{1\rho}$ data were fitted to a stretch exponential of the form $\exp[-(\tau/T_{1\rho})^\alpha]$. Temperature calibrations of the MAS probes (below 650 K) were performed with the ^{207}Pb chemical shift thermometer of $\text{Pb}(\text{NO}_3)_2$,^{47,48} and by following the ^{63}Cu resonances of Cu^I and Cu^{II}Br across the γ -to- β phase transition at 642 and 658 K, respectively.^{49,50} Temperature calibration of the laser heated NMR probe was carried out by direct measurements of the melting points of

reference samples.^{45,46} All temperatures reported are actual sample temperatures and have an estimated accuracy of ± 5 K (below 294 K), ± 10 K (between 294 and 420 K), ± 20 K (between 420 and 650 K) and ± 30 K (above 650 K on the static laser probe).

Spectra were referenced to 10 M LiCl in D₂O (for ^{6,7}Li shifts) and H₂O (for ¹⁷O shifts) at 0 ppm.

2.5. Processing and AC Impedance Spectroscopy. The synthesized powder samples were ball-milled overnight in ethanol (350 rpm, Fritsch Pulverisette 7 Planetary Mill) and dried at 350 °C under flowing dry O₂ for 24 h. The powders were then pressed uniaxially in to pellets of 10 mm diameter and subjected to isostatic pressing at 200 MPa using an Autoclave Engineers Cold Isostatic Press. The resulting pellets were sintered at 900 °C under O₂ for 36 h, and a density of $\approx 67\%$ was obtained. X-ray diffraction showed no impurity phases were present in the pellet. The samples were coated with Ag paste, followed by heating to 100 °C for 1 h to ensure bonding to the sample surface. Conductivity measurements were then performed in dry, ambient and wet air (the inlet gas being bubbled through water at room temperature resulting in water partial pressure of $P_{\text{H}_2\text{O}} \approx 0.03$ atm) by AC impedance spectroscopy (Solartron 1260A impedance analyzer) in the frequency range from 0.01 to 3×10^7 Hz with a perturbation of 20 mV. The impedance data were analyzed using ZView software.

3. RESULTS

3.1. Synthesis and Chemical Analysis. Initial synthetic effort concentrated on the introduction of A-site vacancies into SrLi_{0.4}W_{0.6}O₃²⁴ with the aim of subsequently filling them partially with Li. This was addressed by replacing Sr²⁺ with 2/3 La³⁺ to form the series Sr_{1-3x/2}La_xLi_{0.4}W_{0.6}O₃. These reactions led to multiphase products, but it was noted that solid state reactions at the target composition La_{2/3}Li_{0.4}W_{0.6}O₃ with a large amount of excess Li to avoid Li loss during synthesis resulted in the formation of Li₄WO₅ and a new phase matching a monoclinic distorted perovskite by indexing the PXRD pattern. Sonication in nitric acid converted the Li₄WO₅ to the water-soluble Li₂WO₄, allowing purification of the perovskite phase by washing in water. Initial ICP-OES and TEM-EDX analysis suggested that this phase had a composition close to La₃Li₃W₂O₁₂, and subsequent synthesis at 900 °C for 65 h from oxide starting materials at this nominal composition resulted in phase pure samples without the need for the removal of impurities by washing. This synthetic route was used for all materials measured in the paper.

The metal content of La₃Li₃W₂O₁₂ was measured by ICP-OES, and after normalizing the metal concentrations to a total of eight cations, the determined composition is La_{3.020(81)}Li_{2.975(61)}W_{2.004(9)} (Table S1 in the Supporting Information). In addition, TEM-EDX analysis was used to measure the La/W ratio of ten individual grains of the same sample, and shows a distribution of La/W ratios with a mean of 1.52(8) (Figure S1). The nominal stoichiometric composition of La₃Li₃W₂O₁₂ lies within the standard deviation of the composition measured by both ICP-OES and TEM-EDX, and will be used throughout the rest of the paper.

3.2. Diffraction Experiments. **3.2.1. Cell Indexing and B-Site Cation Ordering by Powder X-ray Diffraction.** The reflections from the room temperature SXRD pattern of La₃Li₃W₂O₁₂ were indexed to a monoclinic cell represented by a $\sqrt{2}a_p \times \sqrt{2}a_p \times 2a_p$ expansion of the cubic perovskite subcell (of lattice parameter a_p), and its systematic absences were found to be consistent with space group $P2_1/n$. A corresponding Pawley refinement fitted all of the observed peaks with refined unit cell dimensions $a = 5.544\ 35(3)$ Å, $b = 5.611\ 14(3)$ Å, $c = 7.888\ 43(4)$ Å and $\beta = 90.0982(2)^\circ$ (Figure

S2). The small monoclinic distortion is difficult to resolve by laboratory PXRD but is clearly resolved by SXRD (e.g., the splitting of the 101 and 10 $\bar{1}$ peaks, see inset in Figure S2). The combination of a monoclinic $\sqrt{2}a_p \times \sqrt{2}a_p \times 2a_p$ unit cell with $P2_1/n$ symmetry is characteristic of cryolite-type double perovskites, where 1:1 (rock-salt type) B cation ordering (further confirmed by the presence of $(0kl)$: $k = 2n+1$ reflections) is combined with a small tolerance factor that induces a $b^-b^-c^+$ type octahedral tilt distortion.⁵¹ The Li containing double perovskite La₂LiSbO₆²⁷ is an example of this class of double perovskites: it contains Li⁺ and a high valency cation (Sb⁵⁺) in a 1:1 ratio on the B sublattice, whereas the A-site is rich in La³⁺. Consequently the structure of La₂LiSbO₆²⁷ was used to derive a preliminary Rietveld model of La₃Li₃W₂O₁₂, with Sb⁵⁺ replaced by W⁶⁺ and the single crystallographically independent A-site populated by La only (in this refinement the occupancy of Li was ignored due to the insensitivity of X-rays to scattering by Li in the presence of W and La). In order to minimize correlation with refined occupancy parameters, constraints were then applied to the thermal parameters such that the three oxide sites were described by a single parameter, and the B-site cations were also described by a single parameter (due to the weak scattering power of Li). Initially, the atomic coordinates and isotropic thermal parameters were refined, with site occupancies fixed to nominal values. The Li/W occupancies of the B-sites were then allowed to refine independently, with the total occupancy at each site constrained to 1, with no constraint on the global composition. The resulting Rietveld fit is shown in Figure 1a, and the final refined parameters are shown in Table S2. These indicate that the B-site Li/W cations are fully ordered, with refined compositions of Li_{1.000(1)}W_{0.000(1)} (2c site) and Li_{0.015(3)}W_{0.985(3)} (2d site) respectively. The refined La/W ratio of 1.522(4) is consistent with the nominal composition and that determined by TEM-EDX and ICP-OES experiments.

3.2.2. Location of A-Site Li⁺ Ions by Powder Neutron Diffraction. The low concentration of Li⁺ ions on the A-site, coupled to their weak X-ray scattering power, precludes their location by PXRD. However, it has proven to be possible to locate partially occupied Li sites in similar systems, such as La_{0.567}Li_{0.3}TiO₃, by using high resolution neutron diffraction (and hence a stronger negative scattering factor for Li) to generate Fourier difference maps.⁵² The provisional structural model obtained by Rietveld refinement against SXRD data (see section 3.2.1), with no Li on the A-site, was used as a starting model in a Rietveld refinement against HRPD neutron diffraction data collected at 5 K in the d -spacing range 0.5–2.1 Å, and also the room temperature data set in the d -spacing range 0.6–2.6 Å, using only the high resolution detector bank (similar to the strategy employed for Li_{0.30}La_{0.567}TiO₃⁵²). The atomic coordinates were refined independently for La and the three oxide sites and isotropic displacement parameters were refined independently for all atoms. This provided a reasonable fit to both data sets ($R_{\text{wp}} = 2.21\%$, $\chi^2 = 3.15$ at 5 K and $R_{\text{wp}} = 4.67\%$, $\chi^2 = 8.29$ at room temperature, see Figure S3). Inspection of the corresponding Fourier difference maps (Figure 2) revealed a single intense negative peak at 5 K, indicative of unmodelled scattering from Li, which is displaced from the La site by 1.03(2) Å approximately parallel to the $[010]_p$ direction. The large displacement of this peak from the La position, and its negative intensity, means that it cannot be accounted for by disorder (either static or dynamic) of the La position. A negative peak was also found at this position in the

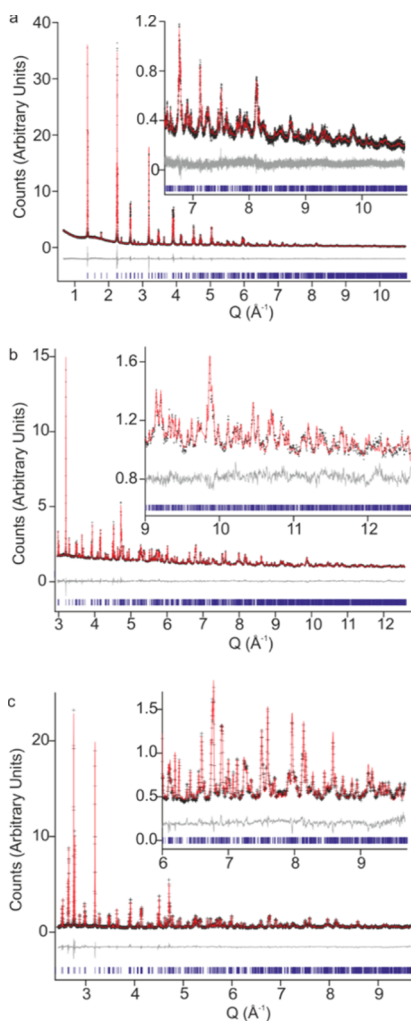


Figure 1. Rietveld refinements of $\text{La}_3\text{Li}_3\text{W}_2\text{O}_{12}$. (a) Simplified structural model (i.e., no A-site Li) refined against high resolution synchrotron X-ray diffraction at ambient temperature. (b) Refinement of the full structural model against PND data from the backscattering bank of HRPD, using a time-of-flight window of 10–110 ms at 5 K. (c) Refinement of the same structural model against PND data from the same detector bank, using a time-of-flight window of 30–130 ms at ambient temperature.

Fourier difference map generated at room temperature, but at this temperature it is difficult to distinguish it from the background features (see Figure 2c): consequently, the 5 K data were used to locate the Li coordinates with greater precision. The model was modified to include Li on this position with an occupancy of 0.25, corresponding to the nominal composition. Isotropic displacement parameters (U_{iso}) were refined independently for each atom, and atomic coordinates for La, Li1 (A-site) and the three oxide sites were also refined independently. The site occupancies were fixed to nominal values for all atoms, as the simultaneous refinement of the occupancy and U_{iso} for Li1 was precluded by a strong correlation between these parameters. This produced a stable refinement (Figure 1b) with an improvement of fit ($R_{\text{wp}} = 2.15\%$, $\chi^2 = 2.969$) for which the refined structural parameters are given in Table S3. Attempts to include Li on other, weaker, negative peaks in the Fourier difference map did not produce stable refinements. The resulting model has A-site Li displaced from the centroid of the O_{12} cage by $0.79(2)$ Å along the

$(110)_p$ direction, where it is coordinated to 4 nearest-neighbor oxygens in a distorted tetrahedron, with Li–O distances in the range $2.11(2)$ – $2.20(2)$ Å (Figure 3). Calculation of the bond valence sums (BVS)³³ at the Li sites gives values of 1.00 at the LiO_6 B-site, and 0.62 at the LiO_4 A-site, indicating that Li is under-bonded in this position. However, this agrees closely with the structure predicted by DFT calculations (Figure 4, see below), implying that this is the most stable position available for A-site Li.

After the Li^+ ions were located at 5 K, the model was tested against room temperature data (Figure 1c). The atomic coordinates and isotropic displacement parameters of the Li1, La and the oxide ions were refined independently, with site occupancies fixed to nominal values, and this was found to produce a stable refinement and an improved fit ($R_{\text{wp}} = 4.54\%$, $\chi^2 = 7.842$). Attempts to include Li atoms on the sites of other negative peaks resulted in unstable refinements with the A-site Li showing a strong tendency to move far from its initial position, and these models were therefore discarded. The refined room temperature structural parameters are shown in Table S4, and the structure (which is isostructural with the 5 K model) is illustrated with the local coordination of A-site Li in Figure S4. Note that, for clarity, the detailed discussion of the $\text{La}_3\text{Li}_3\text{W}_2\text{O}_{12}$ structure (section 4) refers only to the 5 K model.

3.3. Computation. **3.3.1. Location of A-Site Li.** The experimentally determined unit cell of $\text{La}_3\text{Li}_3\text{W}_2\text{O}_{12}$ contains four A-sites, three occupied by La on average, and one by Li. To aid in the determination of the likely location of A-site Li in $\text{La}_3\text{Li}_3\text{W}_2\text{O}_{12}$, DFT calculations in the crystallographic unit cell were performed starting from the refined structure of $\text{La}_3\text{Li}_3\text{W}_2\text{O}_{12}$, with a single A-site Li initially placed on the same site as determined for La. Upon structural relaxation, the A-site Li was displaced away from the La site by 0.4 Å along the b axis to a new site, **A1** (Figure 4a,b), close to that determined by low temperature PND. In this site, which is 4-fold coordinated to O atoms, Li sits in the base of a distorted tetrahedron, with three short bonds (2.00 , 2.04 and 2.08 Å), and one long bond to the apex of the tetrahedron (2.39 Å). The calculated BVS for Li at **A1** is 0.77 , slightly lower than that of the two B-site Li atoms (0.81 and 0.90). As DFT calculations using the generalized gradient approximation are known to overestimate bond lengths, and consequently underestimate BVS, site **A1** appears to be a reasonable coordination environment for the A-site Li. No normal modes with imaginary frequencies are calculated for this structure, showing that it is a true minimum on the potential energy surface at 0 K.

AIMD calculations were performed to investigate the possibility that Li may reside in different coordination environments within a single O_{12} cage around the A-site. Taking the previously calculated cell with Li on site **A1**, a 23 ps AIMD run was performed at room temperature (298 K) using a 1 fs time-step. The trajectory of the A-site Li atom clearly shows that the atom does not simply oscillate around site **A1**, rather it is able to access a large region of space around the center of the O_{12} cage (Figure 4c). A Li density map was constructed, by placing a Gaussian function at each point in space visited by Li during the 23 ps trajectory (Figure 4d). This map, which reflects the amount of time spent by Li in any location, shows that there are other sites in which the A-site Li spends an appreciable amount of time.

Performing standard structural optimization calculations with the A-site Li on these sites within the O_{12} anion cage, followed by normal mode calculations, results in the determination of

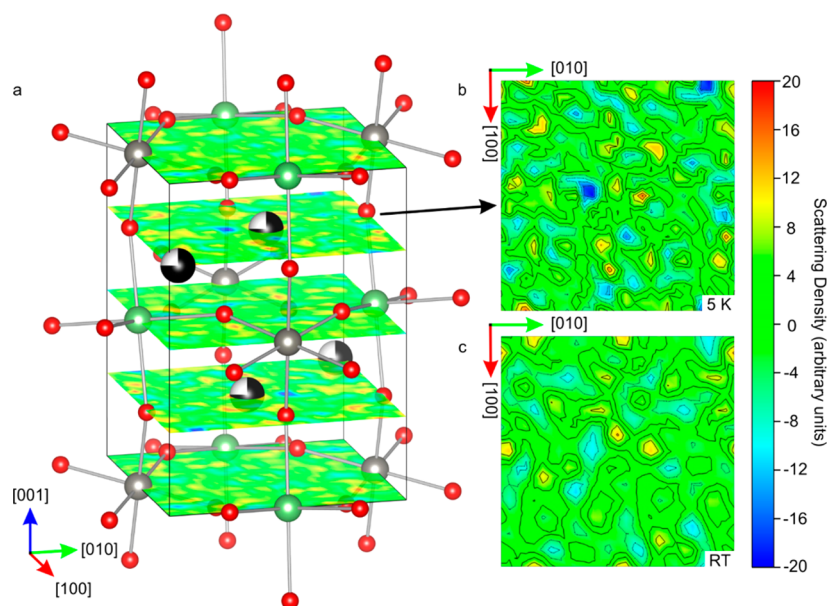


Figure 2. (a) Neutron diffraction Fourier difference map of $\text{La}_3\text{Li}_3\text{W}_2\text{O}_{12}$ sliced in the (001) plane, resulting from a Rietveld model with no A-site Li atoms (superimposed on the map), refined against PND data at 5 K. Atom colors: La in black, Li in green, W in gray, O in red. (b) Individual slice through $z = 0.75$ at 5 K, showing an intense negative peak (blue) which corresponds to unmodelled Li scattering intensity on the A-site. (c) Individual slice through $z = 0.75$ at ambient temperature, resulting from a Rietveld model with no A-site Li atoms, showing only weak negative peaks that are difficult to distinguish from the background.

two more A-site positions which are minima on the 0 K potential energy surface, A2 and A3 (Figure S5). The $\text{La}_3\text{Li}_3\text{W}_2\text{O}_{12}$ structure with A-site Li on either of these two sites is 0.04 eV/FU higher in energy than with Li in A1, but at room temperature AIMD shows that all three sites are occupied for some time. The A-site Li is coordinated to four O atoms on site A2 as on site A1, but Li on site A3 has three short Li–O bonds forming a roughly trigonal planar geometry (Figure S5), though three longer Li–O distances between 2.6 and 3.0 Å may also contribute to stabilizing Li on this site. Nudged elastic band (NEB) calculations were performed to determine the barriers to Li atom hopping between sites A1, A2 and A3. The calculated barriers between A1 and A2, and A1 and A3 are 0.08 and 0.07 eV/FU, respectively (Figure 4e). These barriers are around $3k_{\text{B}}T$ at room temperature, and small enough to allow appreciable hopping between sites even on the picosecond time scale.

3.3.2. Local A-Site Ordering. Refinement of SXRD data shows that the La atoms are randomly distributed over all A-sites, with a partial occupancy of 0.75. There is often a trend toward La ordering in related systems,^{9,53–58} though this is sometimes only seen at the local scale.⁵⁹ To assess the likelihood of local A-site ordering between La and Li in $\text{La}_3\text{Li}_3\text{W}_2\text{O}_{12}$, 128 unique La/Li distributions were generated in a $2 \times 2 \times 1$ supercell using the site occupancy disorder program,⁶⁰ and the resulting supercells structurally optimized using DFT.

Configurations C1 and C2, along with the next most stable configuration, C3 (Figure S6), were used to calculate ^6Li and ^{17}O NMR parameters for comparison with the experimental results in section 3.4.

The energies of the configurations are distributed over a relatively small energy range of 0.43 eV/FU. Two energetically degenerate configurations are found to be the most stable, C1 and C2 (Figure 5). Both configurations show ordering of A-site Li into distinct columns through the structure, running along

the b axis in C1 and the c axis in C2, resulting in A-site layers which are fully occupied by La. The alternation of fully La occupied A-site layers with mixed La/Li or La/vacancy layers has been observed in related perovskites, with long-range ordering present in $\text{La}_{2/3-x}\text{Li}_{3x}\text{TiO}_3$,⁵⁵ $\text{La}_{1/3}\text{NbO}_3$,⁵⁵ $\text{La}_4\text{Mg}_3\text{W}_3\text{O}_{18}$ ⁵⁶ and $\text{La}_6\text{Mg}_4\text{Ta}_2\text{W}_2\text{O}_{24}$,⁶¹ and short-range ordering present in $\text{La}_{5/3}\text{MgTaO}_6$.⁵⁹ A comparison of other computed configurations of $\text{La}_3\text{Li}_3\text{W}_2\text{O}_{12}$ shows that arrangements in which A-site Li are well separated are generally higher in energy. Assuming a completely random distribution of La and Li on the A-site, each A-site Li would be expected to have an average of 0.75 out of six nearest-neighbor A-sites occupied by Li. A plot of configuration energy versus the average number of Li A-site nearest-neighbors for each Li within a configuration, shows a clear trend, with a low p -value (probability of no correlation) of 2×10^{-9} , toward higher numbers of Li–Li nearest neighbors in more stable configurations (Figure 5). This suggests a preference toward local ordering of La and Li. However, the relatively smooth distribution of configuration energies, and the large number of different configurations within $k_{\text{B}}T$ at the synthetic temperature, prevents long-range ordering into any single ordered configuration, and hence the average structure has a three-dimensional Li distribution.

3.3.3. Generation of A-site Li Vacancy Defects. Motion of Li through $\text{La}_3\text{Li}_3\text{W}_2\text{O}_{12}$ is likely to require the presence of Li vacancy defects within the structure. A-site vacancies in stoichiometric $\text{La}_3\text{Li}_3\text{W}_2\text{O}_{12}$ can be created by hosting two Li atoms on the same A-site. The energy cost of creating such Frenkel defects was calculated by taking configurations C1 and C2 in the $2 \times 2 \times 1$ supercell, and moving one A-site Li atom away from its original site into a site close to another A-site Li atom. After relaxing seven such structures using DFT, the lowest energy structure, a defective C2 configuration (Figure 5e), was 0.39 eV per defect higher in energy than the perfect C2 configuration. The two A-site Li atoms within the same A-site O_{12} cage are located close to the A1 and A2 positions

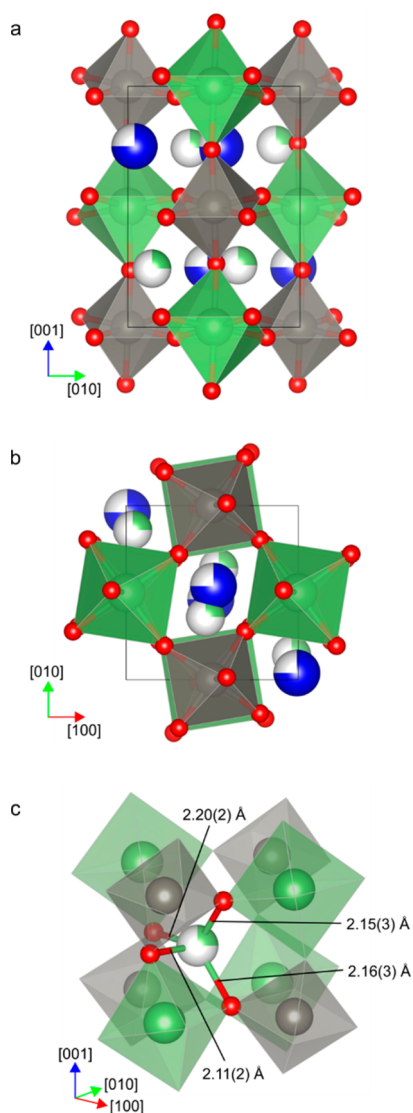


Figure 3. Crystal structure of $\text{La}_3\text{Li}_3\text{W}_2\text{O}_{12}$ from NPD at 5 K. (a) Monoclinic $\sqrt{2}a_p \times \sqrt{2}a_p \times 2a_p$ unit cell viewed along the (100) axis. (b) Unit cell viewed along the (001) axis. (c) A fragment of the unit cell showing the distorted tetrahedral coordination of Li at the A-site. Atom colors: La in blue, Li in green, W in gray, O in red; pie charts signify the occupancies of the sites.

(section 3.3.1), though displaced away from each other increasing the Li–Li separation to 2.6 Å (Figure 5e).

A-site vacancies could also be generated by a slight excess of La (within the experimental uncertainty), forming $\text{La}_{3+x}\text{Li}_{3-3x}\text{W}_2\text{O}_{12}$. Starting from configuration C1 (section 3.3.2), 55 symmetrically unique configurations were generated in the $2 \times 2 \times 1$ supercell, in which one A-site Li atom was replaced with a La atom, and two A-site Li atoms removed. These configurations were relaxed using DFT, and energetically compared to a combination of $\text{La}_3\text{Li}_3\text{W}_2\text{O}_{12}$ and La_2WO_6 . The lowest energy configuration (Figure 5f) gives a defect energy of 0.77 eV per additional La atom, or equivalently 0.39 eV per Li vacancy.

Charge compensation of two Li vacancies by removal of a single oxide ion was investigated by calculating the energy of 40 unique arrangements of Li and O vacancies starting from configuration C1. The lowest energy arrangement (Figure 5g) contains a 5-fold coordinated W atom, in a trigonal bipyramidal

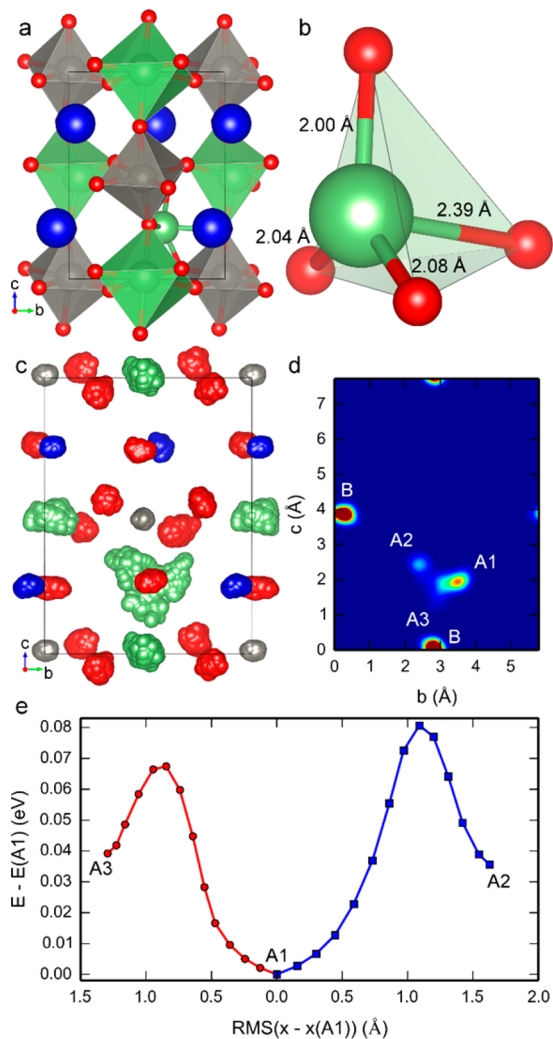


Figure 4. A-site Li positions in $\text{La}_3\text{Li}_3\text{W}_2\text{O}_{12}$ calculated by DFT. Position A1 is shown in panel (a), and the coordination spheres of the A-site Li atom are labeled with Li–O distances below 2.5 Å in panel (b). The atomic positions during a 23 ps trajectory of a room temperature AIMD run are plotted every 10 fs in panel (c). A Li density map of this trajectory in panel (d) shows that the A-site Li resides in different positions within the cell. These are labeled according to the corresponding stable A-site positions determined by DFT: A1, A2 and A3. Atom colors: La in blue, Li in green, W in gray, O in red. The energies of the lowest energy pathways between site A1 and sites A2 and A3 were calculated using the NEB method, and are plotted in panel (e) as a function of the root-mean-square difference in positions between each image structure and the lowest energy structure, A1.

coordination geometry. It is 1.11 eV less stable than the defect free structure, a defect energy of 0.55 eV per Li vacancy.

Another potential compensation mechanism is the replacement of a B-site Li with a B-site W, and five A-site Li vacancies, but it is not feasible to model this using the present supercell methodology. By necessity, the calculations presented here are performed in relatively small supercells, and therefore represent an unrealistically high defect concentration, nevertheless they reveal that Li vacancies can be formed with an energy penalty below $5k_B T$ at the synthesis temperature of $\text{La}_3\text{Li}_3\text{W}_2\text{O}_{12}$, and are therefore likely to exist at low concentrations.

3.3.4. Li Motion between O_{12} Cages. The motion of A-site Li atoms between neighboring O_{12} cages was investigated by

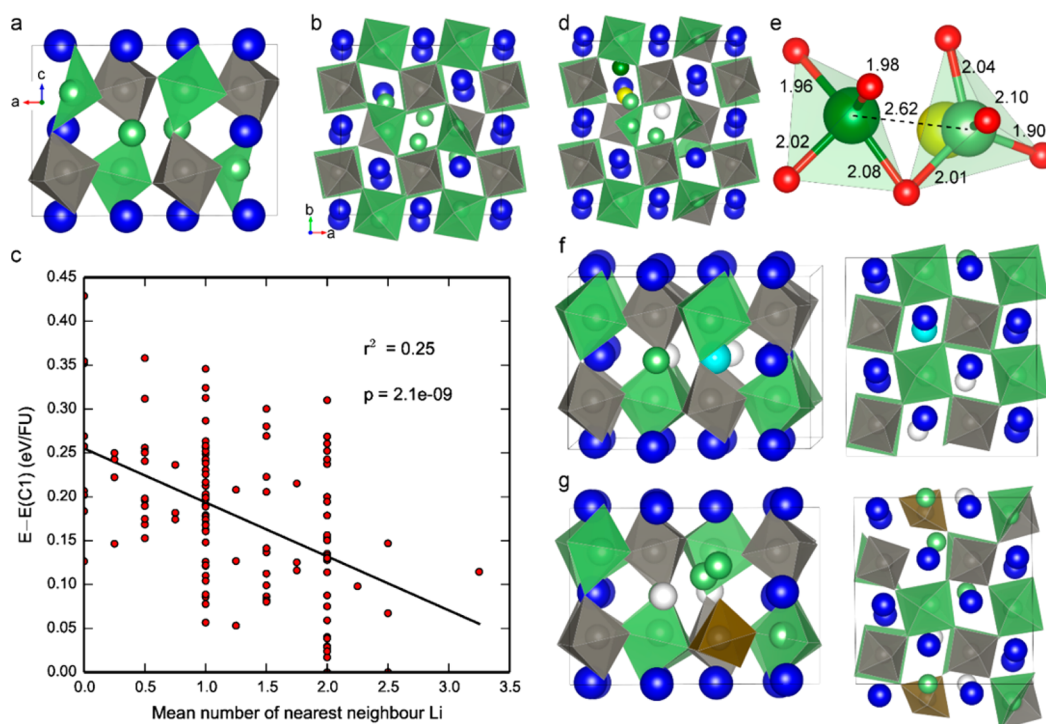


Figure 5. Two most stable arrangements of A-site La and Li in a $2 \times 2 \times 1$ supercell and the computed structure of Li vacancy defects: (a) configuration C1 and (b) configuration C2. Structures are viewed down the axis along which A-site Li forms columns, with the A-site Li in the center of the cell. A-site layers fully occupied by La can be seen at the edges of the cells. B-site atoms and their coordinating O atoms are shown as polyhedra. (c) The energy of 128 configurations relative to configuration C1 is plotted against the mean number of Li A-site nearest neighbors for each A-site Li within the structure. The black line is a fit by linear regression to the data, showing correlation between the stability of configuration and short-range ordering of the A-site Li atoms. A random distribution of La and Li on the A-site gives a value of 0.75 for the number of nearest neighbors, and Li in 1D columns have two Li A-site nearest neighbors. (d) Frenkel defect in configuration C2. The Li vacancy site is shown in white, the new interstitial Li A-site in dark green, and the original A-site Li position in yellow. The coordination environments of the two Li sharing the same A-site are shown in panel (e), with bond distances and the Li–Li separation shown in Angstroms. (f) Three A-site Li atoms in configuration C1 are replaced with one La (cyan) and two vacancies (white). (g) Two A-site Li vacancies (white) in configuration C1 are compensated by the removal of one oxygen atom, forming a 5-fold trigonal bipyramid coordinated W atom (brown). B-site atoms and their coordinating O atoms are shown as polyhedra. Atom colors: La in blue, Li in green, W in gray. Oxygen atoms have been omitted for clarity, except in panel (e) where they are shown in red.

performing a 20 ps AIMD run at 673 K within a supercell containing a Frenkel defect. The vacancy and interstitial Li atoms were separated sufficiently to prevent recombination and removal of the defect. Figure 6 shows that even on the relatively small time scale of 20 ps, hopping between occupied and vacant A-sites in neighboring O_{12} cages is observed, along with considerable motion of the interstitial Li atom within each cage. Cage-to-cage hopping occurs through a window of four O atoms in a roughly rhomboid configuration. Frenkel defects will thus give rise to long-range diffusion at temperatures where finite ionic conductivity is observed in experiment. In addition a single hopping event was observed from an occupied Li B-site to a neighboring vacant A-site and back again (Figure 6c), showing that exchange between the A-site and B-site is possible at this temperature.

To investigate the energetics of Li^+ ion hopping in more detail, a series of constrained DFT relaxations were performed. The position of a W atom and the y -coordinate of the A-site Li atom in the channel containing the A-site vacancy were fixed in the supercell used in the AIMD run described above. The cell and all other atomic positions were then allowed to relax. This process was repeated for a range of y -coordinates through the supercell (Figure 6d), producing an energy landscape for the motion of Li through the two A-sites (Figure 6e). The landscape is more complicated than might be expected,

consisting of multiple minima and energy barriers, the configurations of which are shown in Figure S7. The difference in energy between the lowest energy minima and the highest point on the landscape is ~ 0.25 eV, with barriers to individual hopping events in the range of 0.1–0.2 eV. Cage-to-cage hopping of Li atoms is therefore likely to occur through a complicated combination of many shorter range hopping processes between local minima on the energy landscape, rather than single hops between one O_{12} cage and the next. This is consistent with the different stable A-site positions within a single cage calculated in section 3.3.1, and the trajectories shown in the AIMD run (Figure 6a).

3.4. NMR. Solid state NMR has proven itself to be a valuable technique to investigate and understand Li environments and diffusion in fast Li^+ ion conductors, taking advantage of the two stable NMR active isotopes of lithium (6Li and 7Li). 6Li solid-state magic angle spinning (MAS) NMR is widely used for structure investigation because of the high resolution data usually obtained with this isotope. Additionally, it is well-known that there is a correlation between 6Li shift and Li–O coordination^{30,62,63} that permits the characterization of the local Li environments. The Li dynamics are studied with a range of 6Li and 7Li variable temperature NMR experiments.^{8,64–70} The temperature dependence of NMR line width and spin–lattice relaxation times T_1 and $T_{1\rho}$ for both

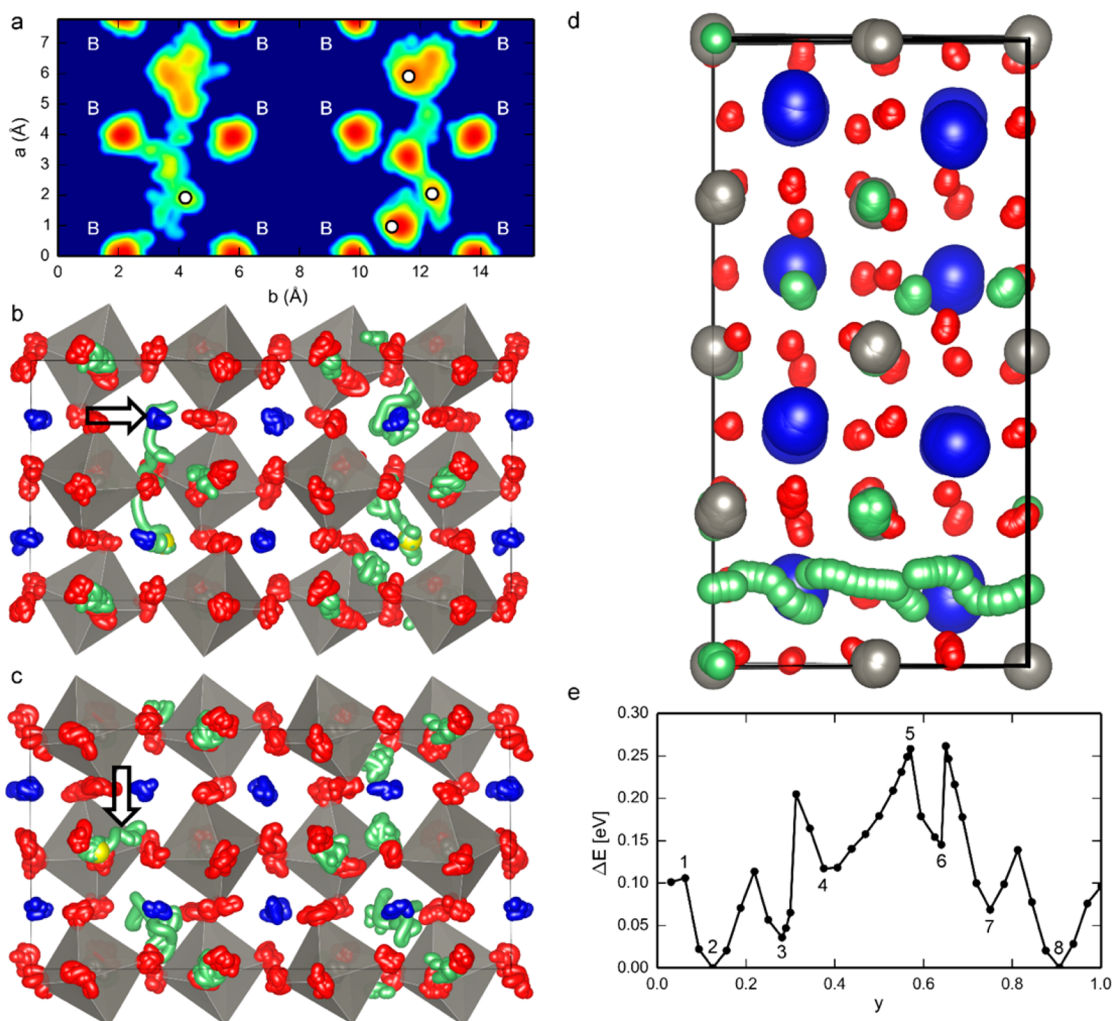


Figure 6. Calculated Li^+ ion dynamics. (a) A Li density map of the Li positions throughout a 20 ps AIMD run at 673 K. The initial locations of A-site Li atoms are shown as white circles. The left half of the cell contains a vacant A-site, and the right half an interstitial A-site Li. B-site Li atoms are labeled with a B. Contours are plotted on a logarithmic scale. (b) The atomic positions between 3 and 4 ps, showing the migration of A-site Li from an occupied O_{12} cage to a vacant one (left, initially vacant site marked with an arrow) and between two interstitial sites within an O_{12} cage (right). (c) The atomic positions between 15 and 16 ps, showing the migration of a B-site Li (yellow sphere) to the neighboring A-site (Li path marked with an arrow). The energy landscape for the migration of Li through two A-sites is calculated with constrained DFT relaxations. (d) The atomic positions from each constrained DFT relaxation are overlaid as the Li was moved through the A-site channel containing an A-site vacancy, showing the path of Li throughout the cell between two O_{12} cages. (e) The relative energy of each relaxed structure is plotted against the fractional y -coordinate of the constrained Li atom. Numbers relate to the atomic configurations shown in Figure S7. Gray polyhedra are the coordination environments of the W atoms, O atoms are shown in red, La in blue and Li in green with yellow spheres marking the positions of the Li atoms at the start of the AIMD run.

Li nuclei are very sensitive to the mobility of Li^+ on the NMR time scale (kHz to MHz), allowing determination of Li jump rates τ^{-1} .

3.4.1. Identification of Two Li Sites with ^6Li MAS NMR Spectroscopy. The room temperature ^6Li MAS NMR spectrum of $\text{La}_3^6\text{Li}_3\text{W}_2\text{O}_{12}$ recorded at 20 T is presented in Figure 7a (see Figure S8 for other conditions), where two Li environments are clearly observed. The spectrum is fitted with two resonances at 0 and -0.4 ppm in a 1:2 ratio, consistent with the A:B site Li ratio proposed in the structural model. Based on the known relationship between ^6Li shift and Li coordination numbers,^{30,62,63} the latter resonance is assigned to LiO_6 whereas the former corresponds to a lower coordinate Li environment. Spectral assignment of this resonance to a specific coordination number is not straightforward given the range of potential shifts for four and five coordinated Li^+ ions. For example, LiO_4 and

LiO_5 sites appear at 0.8 and 0.2 ppm in Li_4SiO_4 respectively,^{62,63} whereas LiO_4 appears around 0.1 ppm in other Li containing silicates.⁶³ These data confirm the presence of both Li atoms in the B-site (LiO_6) and the A-site (LiO_4 or LiO_5) of $\text{La}_3\text{Li}_3\text{W}_2\text{O}_{12}$, consistent with both the experimental diffraction and computational DFT determination of the A-site Li coordination environment.

The three most stable configurations of $\text{La}_3\text{Li}_3\text{W}_2\text{O}_{12}$ in the $2 \times 2 \times 1$ supercells C1, C2 and C3 (section 3.3.2) were used to predict the ^6Li NMR parameters using the GIPAW approach.^{38,39} Li^+ ions at the A-sites in these optimized structures have calculated isotropic shielding values, σ_{iso} of 91.0 ± 0.1 ppm (and calculated isotropic chemical shifts $\delta_{\text{iso,cs}} = -0.6$ ppm) and those at the B-sites of 91.5 ± 0.1 ppm (and $\delta_{\text{iso,cs}} = -1.0$ ppm, Figure S10). Because the experimentally observed shifts are expected to be proportional to $-\sigma_{\text{iso}}$,⁷¹ this

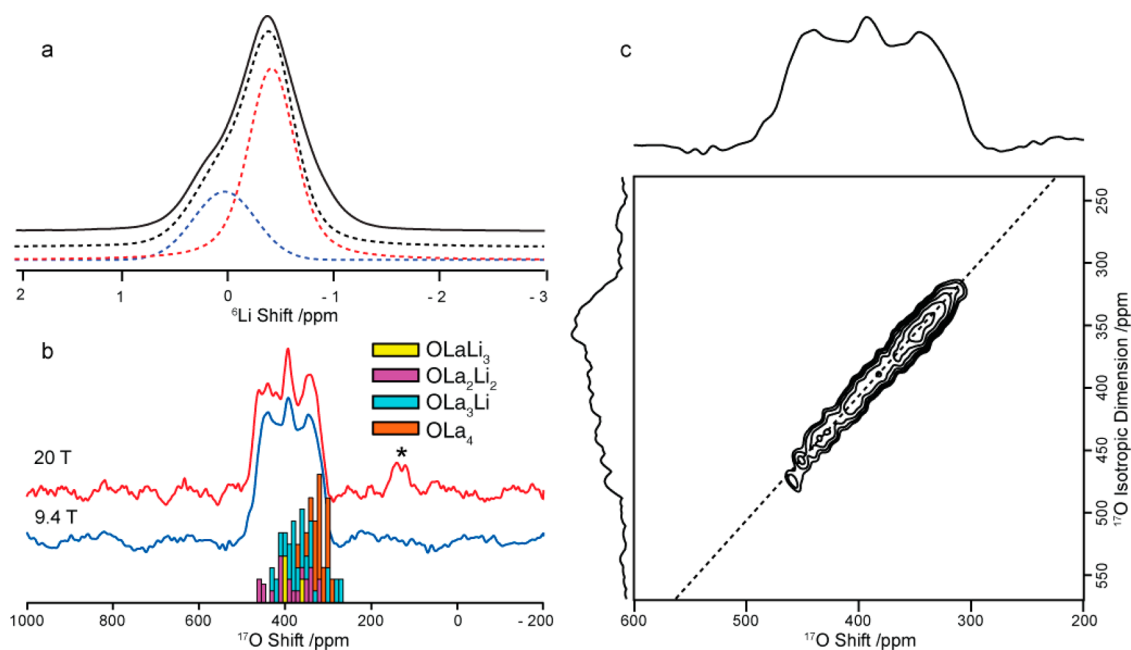


Figure 7. NMR structural investigation of $\text{La}_3\text{Li}_3\text{W}_2\text{O}_{12}$. (a) ^6Li magic angle spinning (MAS) NMR spectra of $\text{La}_3^6\text{Li}_3\text{W}_2\text{O}_{12}$ recorded at 20 T under MAS at 10 kHz. Black dashed lines represent line shape simulation using two different ^6Li resonances at 0 ppm (blue dashed line) and -0.4 ppm (red dashed line) corresponding to A-site (LiO_4 or LiO_5) and B-site (LiO_6) local environments, respectively. ^6Li MAS NMR spectra recorded at 9.4 T and faster MAS are given in Figure S8. (b) ^{17}O Hahn echo NMR spectra of $\text{La}_3\text{Li}_3\text{W}_2^{17}\text{O}_{12}$ recorded at 9.4 T under MAS at 13 kHz (blue) and at 20 T under MAS at 20 kHz (red). The histogram represents the number of oxygen atoms as a function of the calculated GIPAW^{38,39} ^{17}O shifts for the 96 oxygen atoms of the $2 \times 2 \times 1$ cell of $\text{La}_3\text{Li}_3\text{W}_2\text{O}_{12}$ within the three lowest energy structures C1, C2 and C3 (OLa₃Li₃, OLa₂Li₂, OLa₃Li and OLa₄ oxygen environments are given in yellow, purple, cyan and orange, respectively). The calculated ^{17}O shifts appear to be weakly correlated with the number of La^{3+} ions around a single O^{2-} ion (see Figure S9). Asterisks (*) denote spinning sidebands. (c) ^{17}O 2D z-filtered 3QMAS spectrum of $\text{La}_3\text{Li}_3\text{W}_2^{17}\text{O}_{12}$ recorded at 9.4 T and under MAS at 13 kHz. The diagonal dotted line represents the isotropic correlation line. Left: isotropic projection of the 2D 3QMAS data. Top: ^{17}O Hahn echo NMR spectra of $\text{La}_3\text{Li}_3\text{W}_2^{17}\text{O}_{12}$.

is consistent with the assignment of the peaks at 0.0 and -0.4 ppm as A-site Li (LiO_4) and B-site (LiO_6) environments.

3.4.2. ^{17}O NMR Spectroscopy. The ^{17}O Hahn echo spectra obtained for $\text{La}_3\text{Li}_3\text{W}_2^{17}\text{O}_{12}$ at 9.4 and 20 T show a pattern consisting of multiple overlapping peaks spanning 300 to 500 ppm (Figure 7b). Both spectra have similar line widths and no further line narrowing is seen at high field, as expected for ionic solids.⁷² No further spectral resolution is obtained in the 2D 3QMAS NMR spectrum obtained at 9.4 T (Figure 7c) which shows signal along the isotropic diagonal and is indicative of a large distribution of chemical shifts which can be associated with structural disorder.

The accuracy of the calculation of NMR parameters using the GIPAW^{38,39} approach has greatly increased and the method can be used with confidence as a predictive tool for spectral assignments of oxide materials.^{71,73} GIPAW calculations were used to determine the expected experimental shifts arising from the various local oxygen environments OLi₃La, OLa₂Li₂, OLa₃Li and OLa₄ in $\text{La}_3\text{Li}_3\text{W}_2\text{O}_{12}$. Calculated ^{17}O shifts δ are distributed over the 300–480 ppm range (Figure 7b) and agree well with the experiment shifts observed in $\text{La}_3\text{Li}_3\text{W}_2^{17}\text{O}_{12}$. Note that the quadrupolar interaction contribution to the shifts is negligible as evidenced by the absence of field dependence of the ^{17}O NMR spectra and confirmed by the small calculated quadrupolar induced shift of <10 ppm, as expected for ionic solids (see SI).⁷² There is a weak correlation between the predicted shifts and the different number of A-site Li^+ ions coordinated to a single O^{2-} ion, the higher shift obtained corresponding to the larger number of coordinated Li^+ ions (Figure S9). This trend is expected due to the smaller chemical

shieldings (and hence larger shifts) created around oxygens by the smaller four-coordinated Li^+ than La^{3+} (ionic radii of 0.76 and 1.03 Å, respectively).⁷⁴

3.4.3. Li^+ Ion Mobility: ^7Li Line Shape Analysis. Information on the Li^+ ion dynamics was initially obtained from motional narrowing of the static ^6Li and ^7Li NMR spectra as a function of temperature. The variable temperature ^7Li NMR spectra of $\text{La}_3\text{Li}_3\text{W}_2\text{O}_{12}$ and ^6Li NMR spectra of $\text{La}_3^6\text{Li}_3\text{W}_2\text{O}_{12}$ obtained at 9.4 T are shown in Figure 8. Below room temperature, the ^7Li static NMR spectra show the anticipated line shape expected for a spin 3/2 nucleus with a dipolar broadened central line (full width at half-maximum of ~ 4 kHz) at around 0 ppm corresponding to the $+1/2 \leftrightarrow -1/2$ central transition, and a very broad resonance spanning ~ 300 ppm (~ 50 kHz) corresponding to the $3/2 \leftrightarrow 1/2$ and $-1/2 \leftrightarrow -3/2$ satellite transitions. The broadening of the central transition is due to the strong $^7\text{Li}-^7\text{Li}$ homonuclear dipolar interaction and is averaged out as the temperature is increased due to greater Li^+ ion mobility (Figure 8c), yielding motional narrowing of NMR line widths. Similarly, the ^6Li static NMR lines of $\text{La}_3^6\text{Li}_3\text{W}_2\text{O}_{12}$ are slightly broadened (~ 1.4 kHz) below room temperature and narrow with increasing temperature to ~ 0.7 kHz at ~ 600 K and ~ 0.5 kHz above ~ 900 K. The onset of motional narrowing occurs at ~ 300 K for both ^6Li and ^7Li . At the inflection point of the temperature dependent line narrowing experiment, the Li^+ jump rates τ^{-1} are estimated from the NMR line width in the low temperature rigid-lattice regime $\Delta\omega_{\text{rigid lattice}}$ and yield values of $\sim 9 \times 10^3 \text{ s}^{-1}$ and $\sim 3 \times 10^4 \text{ s}^{-1}$ at 400 and 420 K from ^6Li and ^7Li data, respectively.

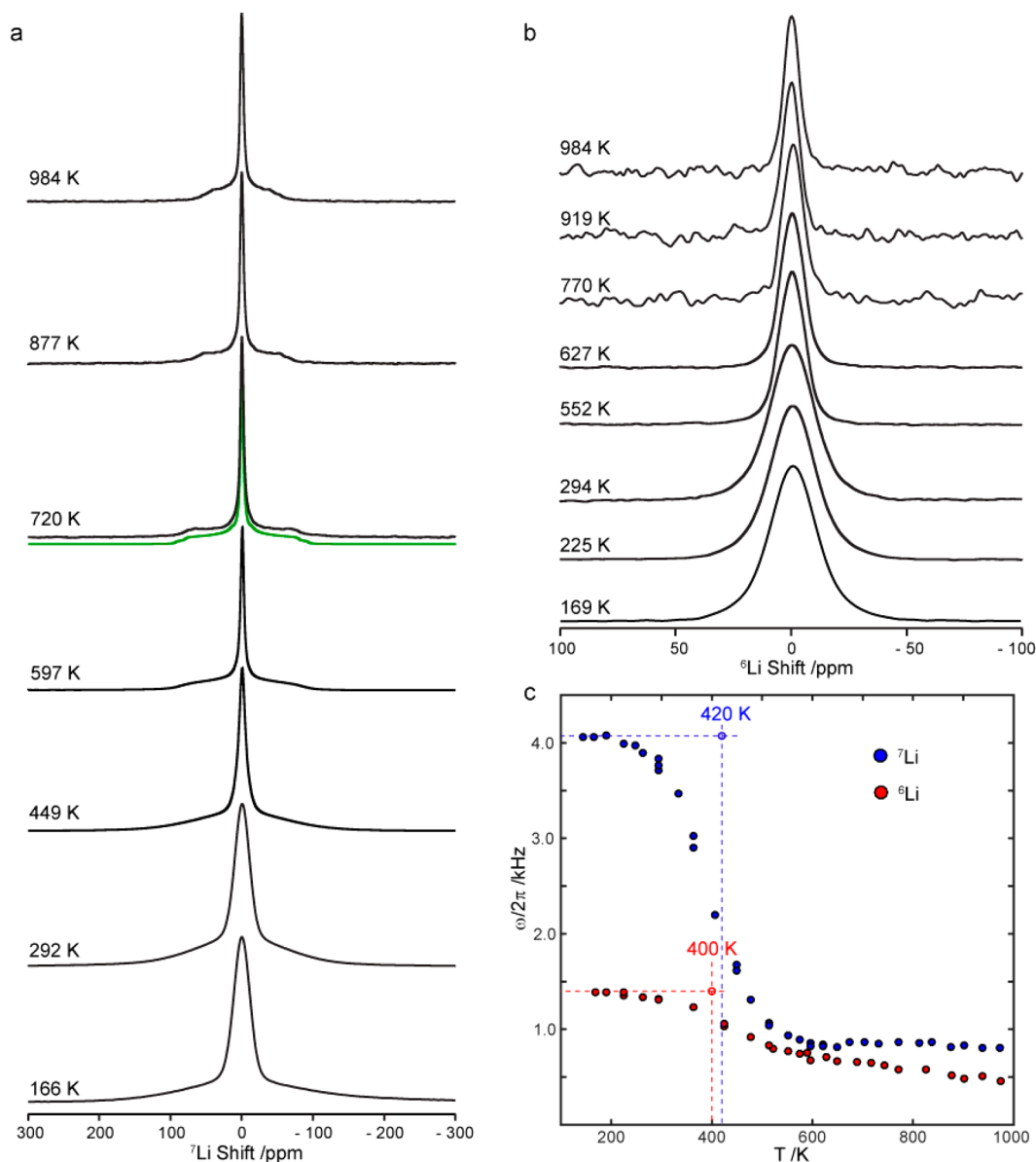


Figure 8. Li^+ dynamics obtained from NMR motional narrowing. (a) ${}^7\text{Li}$ static NMR spectra of $\text{La}_3\text{Li}_3\text{W}_2\text{O}_{12}$ and (b) ${}^6\text{Li}$ static NMR spectra of $\text{La}_3\text{Li}_3\text{W}_2\text{O}_{12}$ as a function of temperature. The green spectrum in panel (a) corresponds to a line shape simulation. (c) Temperature dependence of the ${}^6\text{Li}$ (red) and ${}^7\text{Li}$ (blue) NMR line widths of $\text{La}_3\text{Li}_3\text{W}_2\text{O}_{12}$. The vertical and horizontal dashed lines give the temperatures corresponding to the inflection point of the ${}^6\text{Li}$ line narrowing experiments and the rigid-lattice line width $\Delta\omega_{\text{rigid lattice}}$ used to determine the Li jump rates τ^{-1} ($\tau^{-1} \approx \Delta\omega_{\text{rigid lattice}}$), respectively, and are guides to the eyes.

In the fast motional regime above 420 K, the static ${}^7\text{Li}$ NMR spectra show motionally narrowed NMR lines and the typical broad powder pattern line shape characteristics of a spin 3/2 nucleus with the clear discontinuities associated with the satellite transitions. At 720 K, these singularities are observed at ~ -100 and $+100$ ppm (Figure 8a) from which a quadrupolar coupling constant C_Q of 30 kHz can be estimated. As the temperature is increased to 984 K, the broad static pattern gradually narrows through a continuous averaging of the electric quadrupolar interactions by Li^+ ion motion. It is potentially expected that at higher temperature the satellite transitions would completely narrow and vanish due to increasing Li^+ ion mobility. However, this regime is not obtained here due to the decomposition of $\text{La}_3\text{Li}_3\text{W}_2\text{O}_{12}$, or its reaction with the BN crucible, above 1000 K under the reducing N_2/Ar atmosphere of the high temperature laser

heated NMR probe used (see Figure S11 for stability test of $\text{La}_3\text{Li}_3\text{W}_2\text{O}_{12}$ monitored by PXRD).

3.4.4. Li^+ Ion Mobility: ${}^{6,7}\text{Li}$ Spin–Lattice Relaxation Rates. Figure 9a shows the temperature dependence of the ${}^6\text{Li}$ and ${}^7\text{Li}$ spin–lattice relaxation rates in the laboratory and rotating frames, T_1^{-1} and $T_{1\rho}^{-1}$, providing Li^+ ion dynamics with frequencies on the order of the Larmor ($\nu_0 = 59$ and 156 MHz for ${}^6\text{Li}$ and ${}^7\text{Li}$) and spin-lock frequencies ($\nu_1 = 8$ and 14 kHz), respectively, resulting from fluctuations of the local magnetic dipolar or electrical quadrupolar interactions induced by Li^+ ion motion. At temperature below 250 K, the T_1^{-1} and $T_{1\rho}^{-1}$ values are relatively constant, showing little Li^+ ion motion. As the temperature is increased to 260 K, the T_1^{-1} and $T_{1\rho}^{-1}$ rates measured for both ${}^6\text{Li}$ and ${}^7\text{Li}$ become longer and are indicative of a slow motional regime (where $2\pi\nu_0\tau_c$ and $2\pi\nu_1\tau_c \gg 1$ with τ_c the correlation time of the motion). Here, both T_1^{-1} and

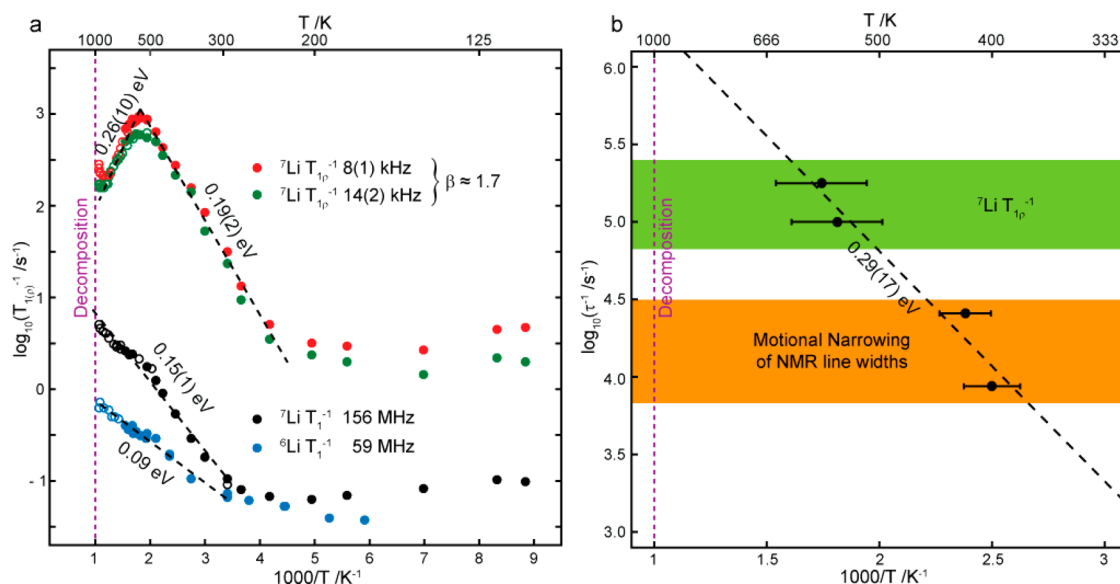


Figure 9. Li^+ ion dynamics obtained from NMR relaxometry. (a) Arrhenius plot of the spin–lattice relaxation rates T_1^{-1} obtained at $\nu_0({}^6\text{Li}) = 59$ MHz (blue) on $\text{La}_3{}^6\text{Li}_3\text{W}_2\text{O}_{12}$ and $\nu_0({}^7\text{Li}) = 156$ MHz (black), and the spin–lattice relaxation rates in the rotating frame $T_{1\rho}^{-1}$ obtained at $\nu_1({}^7\text{Li}) = 8$ kHz (red) and 14 kHz (green) on $\text{La}_3\text{Li}_3\text{W}_2\text{O}_{12}$. Filled and empty black circles refer to data obtained with the MAS probes and the laser heated static probe, respectively. The slight anomaly seen at ~ 600 K for ${}^7\text{Li } T_{1\rho}^{-1}$ data perhaps results from the change in NMR probe used to perform the experiment. Dashed lines represent the range where the activation energies E_a and the deviation from BPP theory defined by β (see text) are determined. (b) Arrhenius plot of Li jump rates τ^{-1} extracted from motional narrowing of NMR line width (Figure 8) and the NMR relaxometry data. Horizontal error bars represent the estimated errors of temperature gradient and peak position of $T_{1\rho}^{-1}$ maximum. Vertical error bars are within the size of the symbols. Note that at around 800 K, $T_{1\rho}^{-1}$ minima are seen and may correspond to a different Li^+ dynamics mechanism, which is not quantitatively accessible due to sample decomposition at the higher temperatures where data would be needed to probe fully these processes (see Figure S11).

$T_{1\rho}^{-1}$ rates do not characterize Li^+ ion translational diffusion⁷⁵ but probe local processes such as hopping between local energy minima that contribute to unsuccessful jumps between cages. Activation energies E_a on the order of 0.09–0.19(2) eV are extracted and are similar to those seen in this regime in other Li^+ ion conducting oxides such as $\text{La}_{2/3-x}\text{Li}_{3x}\text{TiO}_3$ ($0.08 < x < 0.167$)^{8,76,77} and cubic $\text{Li}_7\text{La}_3\text{Zr}_2\text{O}_{12}$.⁶⁶

As the temperature is increased further, $T_{1\rho}^{-1}$ maxima are observed at around 550 K and the Li^+ ion jump rates τ^{-1} are on the order of the spin-lock frequency ν_1 ($2\pi\nu_1\tau \approx 0.5$)⁷⁸ yielding values of 1×10^5 and 1.8×10^5 s⁻¹ at 552 and 574 K. At temperatures above these maxima, the T_1^{-1} and $T_{1\rho}^{-1}$ rates decrease (i.e., the material enters the fast motional regime, $2\pi\nu_0\tau_c$ and $2\pi\nu_1\tau_c \ll 1$) and the jump rates τ^{-1} relate to Li^+ translational diffusion.^{79,80} An activation energy of 0.26 ± 0.10 eV is determined from the ${}^7\text{Li } T_{1\rho}^{-1}$ relaxation rates in this regime. The frequency dependence of T_1^{-1} and $T_{1\rho}^{-1}$ rates in the fast motional regime ($2\pi\nu_0\tau$ and $2\pi\nu_1\tau \ll 1$) is well-known to relate to the dimensionality of the diffusion processes.^{65,79}

Figure 9a shows that the ${}^7\text{Li } T_{1\rho}^{-1}$ rates obtained over the 600–800 K temperature range and probed at two different spin lock frequencies ($\nu_1 = 8$ and 14 kHz) are independent of frequency. This is characteristic of 3D diffusion of Li^+ ions in $\text{La}_3\text{Li}_3\text{W}_2\text{O}_{12}$.

The asymmetric behavior of the temperature dependence of the $T_{1\rho}^{-1}$ rates on either side of the maxima has been well documented in the literature for fast ion conductors and disordered materials, and arises from a combination of structural disorder and Coulombic interactions of mobile ions.^{62,79} This yields a deviation from the Bloembergen–Purcell–Pound (BPP)⁸¹ theory of relaxation (which predicts symmetric peaks and a quadratic frequency dependence of the relaxation rates $T_{1\rho}^{-1} \propto \nu^{-2}$) giving in the slow motional regime

($2\pi\nu_1\tau \gg 1$) a frequency dependence of the form $T_{1\rho}^{-1} \propto \nu^{-\beta}$, where the model parameter β ranges between 1 and 2. Our data in the two low temperature flanks of the $T_{1\rho}^{-1}$ rates are indeed frequency-dependent and fit to an exponent $\beta = 1.7$ for ${}^7\text{Li } T_{1\rho}^{-1}$ (using the equation $E_{a,\text{low}} = (\beta - 1)E_{a,\text{high}}$ ⁷⁹ where $E_{a,\text{low}} = 0.19$ eV and $E_{a,\text{high}} = 0.26$ eV are the activation energies on the low and high temperature flanks, respectively). The higher activation energy observed at high temperature accounts for cooperative effects such as long-range Coulombic interactions between charge carriers or structural disorder that produce multiple or correlated hops over longer distances than probed in the lower temperature regime, and corresponds to translational diffusion of Li^+ ions.⁷⁸

The jump rates τ^{-1} extracted from the NMR relaxometry data (that is the two maxima of the ${}^7\text{Li } T_{1\rho}^{-1}$ data, Figure 9a) and the line narrowing experiments (Figure 8c) are plotted against reciprocal temperature (Figure 9b). The fit to the data using an Arrhenius equation of the form $\tau^{-1} = \tau_0^{-1} \exp(E_a/RT)$ is reasonably good and yields an activation energy E_a of 0.29 ± 0.17 eV and a prefactor τ_0^{-1} of $\sim 6 \times 10^7$ s⁻¹. The activation energy determined here is identical to the value seen in the high temperature flank of the ${}^7\text{Li}$ spin–lattice relaxation rate plot (Figure 9a) within experimental error, which suggests that we probe the same diffusive process in both line narrowing and relaxometry experiments.

An NMR conductivity σ_{NMR} can be calculated from this NMR-derived Li^+ ion jump rate τ^{-1} (Figure 9b) by combining the Nernst–Einstein and the Einstein–Smoluchowski equations to give the following expression:

$$\sigma_{\text{NMR}} = \frac{f}{H_R} \frac{Nq^2 a^2}{6k_B T} \frac{1}{\tau}$$

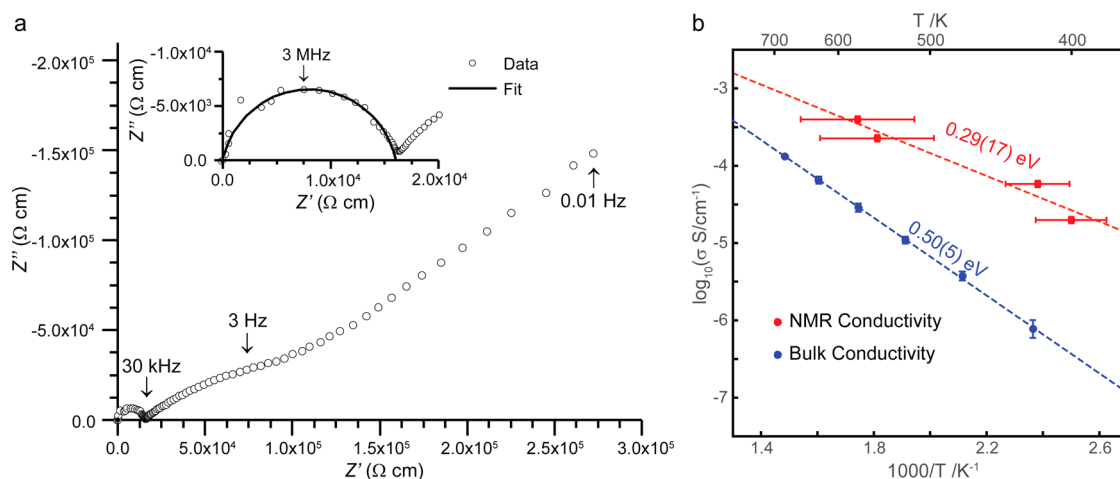


Figure 10. AC impedance data of $\text{La}_3\text{Li}_3\text{W}_2\text{O}_{12}$. (a) Complex impedance plot at 350 °C in air along with the fitting of the bulk arc with an equivalent circuit of resistor-constant phase element (inset). (b) Bulk conductivities σ of $\text{La}_3\text{Li}_3\text{W}_2\text{O}_{12}$ vs temperature obtained from the AC impedance data, and calculated from the NMR Li^+ jump rates τ^{-1} obtained from ^7Li relaxation rates T_{1p}^{-1} and motional narrowing using the Nernst–Einstein–Smoluchowski equations. The horizontal error bar on the NMR conductivity is an estimation of the temperature gradient on NMR probe and the peak position for T_{1p}^{-1} maximum.

where f/H_R is the ratio of the correlation factor and Haven ratio (set to 1 for uncorrelated motion), N is the number of charge carriers (assumed as 1 A-site Li) per unit cell volume (245 \AA^3), q is the ionic charge of Li^+ and a is the average jump distance (taken as $4 \pm 0.2 \text{ \AA}$ for A-site Li–Li distance, see Figure S4), and yields values in the range of $5.8 \times 10^{-5} - 2.2 \times 10^{-4} \text{ S/cm}$ between 400 and 574 K (Figure 10b).

3.5. AC Impedance Spectroscopy. Dilatometry measurements were performed to determine the optimal sintering conditions (Figure S12). No abrupt jump was observed between 50 and 860 °C which suggests that no phase transition occurs in this temperature range. The data show that densification starts at 400 °C and has almost ceased after 24 h at 860 °C. Consequently, pellets were formed by sintering for 36 h at 900 °C and used for AC impedance spectroscopy measurements.

The preliminary impedance data collected under both dry and wet air showed no significant difference, thus showing no evidence of proton conductivity and subsequent measurements were performed in ambient air. The typical complex impedance data for $\text{La}_3\text{Li}_3\text{W}_2\text{O}_{12}$ with a density of 67% is shown in Figure 10a. Data fitting using the ZView software package shows the high frequency semicircle has an associated capacitance of 2.6 pF/cm (corresponding to a relative permittivity of 29) and is therefore assigned to the bulk response. The suppressed arc at intermediate frequency 3 Hz–30 kHz and the low frequency spike are attributed to the electrode response. The low frequency spike at 0.01 Hz is characteristic of the known Warburg impedance associated with Li^+ ion diffusion in the electrode and indicates negligible electronic conduction. Note that the capacitance associated with the arc at 3 Hz–30 kHz is of the order of 10^{-6} F/cm that is too large for a grain boundary response but matches well with an electrode response.⁸² No separate arc associated with the grain boundary response is observed, suggesting the sample is electrically homogeneous. The low density of the sample indicates incomplete ceramic sintering, which may lead to the same electrical response from grain and grain boundary regions, e.g., because there are no compositional changes. The grain boundary arc may also be completely masked by the large electrode arc at 3 Hz–30 kHz.

Thus, only bulk conductivity was extracted from the data. The conductivity of $\text{La}_3\text{Li}_3\text{W}_2\text{O}_{12}$ as a function of temperature (150–400 °C) is shown in Figure 10b. A bulk conductivity at 400 °C of $1.32(3) \times 10^{-4} \text{ S/cm}$ is obtained, which is much lower than those obtained for the LLTO family ($\sigma_{\text{bulk}} \approx 10^{-3} \text{ S/cm}$ at room temperature for $x = 0.1$).⁸³ Arrhenius fits to the conductivities yield an activation energy of $0.50 \pm 0.05 \text{ eV}$, which is greater than the typical activation energy obtained for the LLTO family (between 0.35–0.4 eV).⁸³

4. DISCUSSION

The structure of $\text{La}_3\text{Li}_3\text{W}_2\text{O}_{12}$ differs from those of $\text{La}_{2/3-x}\text{Li}_{3x}\text{TiO}_3$ in several key respects: these are A-site cation ordering, B-site cation ordering and octahedral tilting of the BO_6 framework. LLTO structures show a strong tendency toward layered ordering of Li^+ and La^{3+} cations, which stack in alternating two-dimensional La-rich and La-poor layers, with a degree of ordering that is dependent on thermal history and precise composition.⁸⁴ In contrast, the A-site cations in $\text{La}_3\text{Li}_3\text{W}_2\text{O}_{12}$ are distributed uniformly in three dimensions. The B-site cations in $\text{La}_3\text{Li}_3\text{W}_2\text{O}_{12}$ are fully ordered in a rock salt arrangement, so that each A-site is delimited by four WO_6 octahedra and four LiO_6 octahedra. The framework is distorted by two out-of-phase octahedral tilts of equal magnitude and one in-phase tilt described by the tilt scheme $b^-b^-c^+$: the resulting Li–O–W bond angles lie in the range $152.5(1)^\circ$ – $153.3(1)^\circ$, which are similar in magnitude to those exhibited by other perovskites with this tilt scheme, such as the single perovskite orthoferrites⁸⁵ and the Li containing double perovskite $\text{La}_2\text{LiSbO}_6$.^{27,86} These tilts are larger than those reported in the $\text{La}_{2/3-x}\text{Li}_{3x}\text{TiO}_3$ family of compounds, which host a smaller B-site cation ($r = 0.605 \text{ \AA}$ for Ti^{4+} , versus 0.76 and 0.60 \AA for Li^+ and W^{6+} respectively).⁷⁴ For example, $\text{La}_{0.567}\text{Li}_{0.3}\text{TiO}_3$ and $\text{La}_{0.62}\text{Li}_{0.16}\text{TiO}_3$ each exhibit only a single out-of-phase octahedral tilt with minimum Ti–O–Ti angles of $168.1(3)^\circ$ ⁸⁷ and $168.9(3)^\circ$,⁵⁷ respectively, whereas the most La-deficient member of the series $\text{La}_{0.5}\text{Li}_{0.5}\text{TiO}_3$ exhibits three equivalent out of phase tilts with a Ti–O–Ti angle of $169.6(3)^\circ$.⁸⁸

The nature of the tilts influences the shape of the windows connecting adjacent A-sites. In the $\text{La}_{2/3-x}\text{Li}_{3x}\text{TiO}_3$ system, the

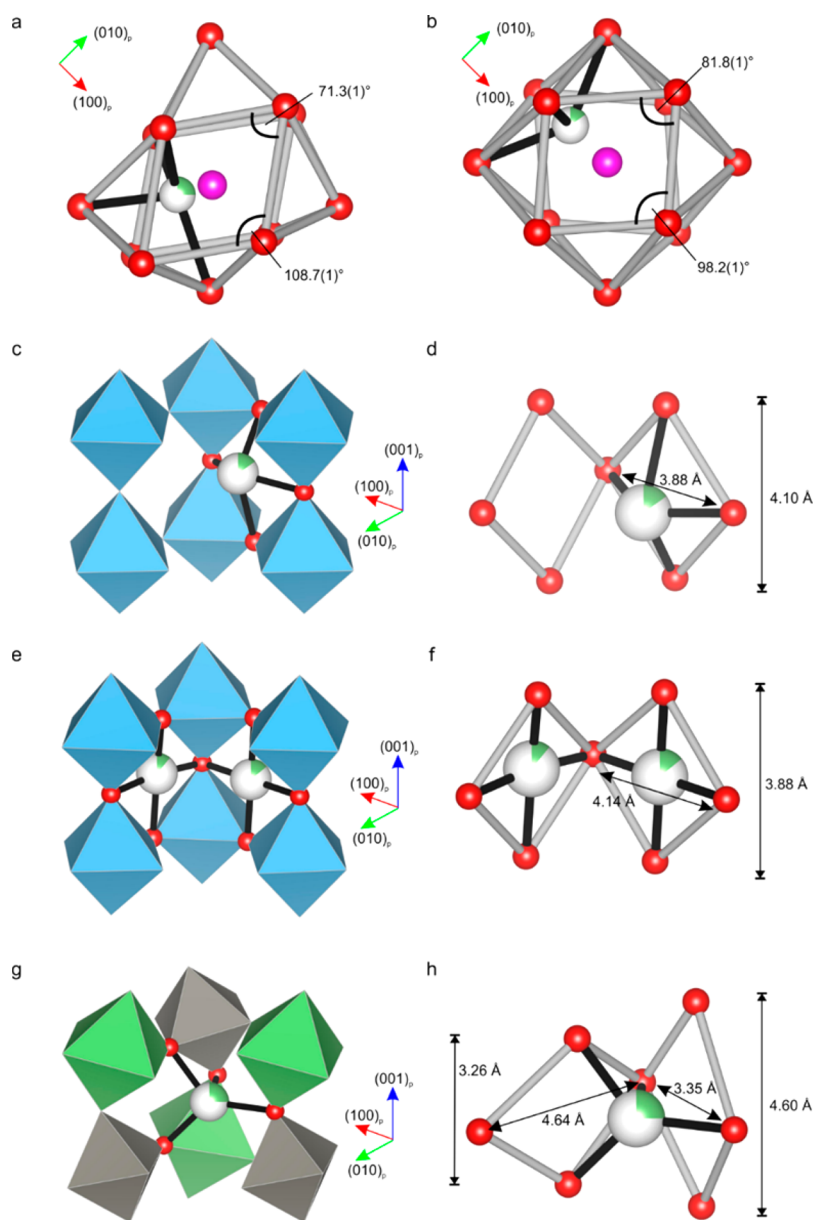


Figure 11. Comparison of the local coordination environments of Li^+ at the A-sites of $\text{La}_3\text{Li}_3\text{W}_2\text{O}_{12}$ (from PND at 5 K) and $\text{Li}_{2/3-x}\text{Li}_{3x}\text{TiO}_3$. (a) The distorted LiO_{12} cuboctahedron in $\text{La}_3\text{Li}_3\text{W}_2\text{O}_{12}$, showing the displacement of Li^+ (green atom) from the O_{12} centroid (magenta atom) approximately along the $(110)_p$ direction toward the vertices of two adjoining BO_6 octahedra, and (b) the near-regular LiO_{12} cuboctahedra in tetragonal $\text{Li}_{0.563}\text{Li}_{0.3}\text{TiO}_3$ ⁸⁴ where Li^+ is displaced from the O_{12} centroid toward the square windows, shown here along $(100)_p$. (c and d) The 4-fold coordination of Li in tetragonal $\text{La}_{0.563}\text{Li}_{0.3}\text{TiO}_3$ ⁸⁴ is formed by four oxides from the same window, and Li is displaced from the plane of the window toward the center of the O_{12} cuboctahedron. (e and f) The 4-fold coordination of Li in rhombohedral $\text{Li}_{0.5}\text{Li}_{0.5}\text{TiO}_3$ ⁸⁸ where Li lies in the planes of the windows. (g and h) The distorted tetrahedral site occupied by Li in $\text{La}_3\text{Li}_3\text{W}_2\text{O}_{12}$ is formed by oxide ions from two adjoining windows due to the distortion of the planar window site by the octahedral tilting. Green octahedra are LiO_6 , gray octahedra are WO_6 , blue octahedra are TiO_6 , red atoms are oxide ions.

relatively weak tilts subject the windows in the O_{12} cages to a small rhombic distortion away from their ideal square geometry in the cubic perovskite structure. For example, in $\text{La}_{0.567}\text{Li}_{0.3}\text{TiO}_3$ the internal angles of the most distorted window are $81.8(1)^\circ/98.2(1)^\circ$,⁸⁷ whereas in $\text{La}_3\text{Li}_3\text{W}_2\text{O}_{12}$ the octahedral tilts impose a far stronger rhombic distortion on the windows, producing internal angles of $71.4(1)^\circ/108.6(1)^\circ$ (Figure 11a,b). The B-site rock salt ordering of Li and W in $\text{La}_3\text{Li}_3\text{W}_2\text{O}_{12}$ has further implications for the distortion of the window sites, because although the individual LiO_6 and WO_6 octahedra in $\text{La}_3\text{Li}_3\text{W}_2\text{O}_{12}$ are both highly regular (their bond length distortion indices^{89,90} are 0.0018 and 0.0015 respec-

tively, and their bond angle variances^{89,91} are 0.328 and 0.309 respectively; these values closely match the range of values exhibited by CaTiO_3 ⁹²), there is a considerable size mismatch between them (the respective octahedral volumes are 12.9 and 9.3 \AA^3 for LiO_6 and WO_6). This size difference between the two B-sites introduces two distinct edge lengths to the windows which distorts the rhombus (produced by octahedral tilting only) to a parallelogram. Despite the large distortion, the windows of $\text{La}_3\text{Li}_3\text{W}_2\text{O}_{12}$ have a greater area than those of $\text{La}_{0.567}\text{Li}_{0.3}\text{TiO}_3$ (8.0 and 7.1 \AA^2 , respectively) because of the large size of the B-site LiO_6 unit.

The nature of this distortion of the windows underpins the difference in the local coordination environment of A-site Li between $\text{La}_3\text{Li}_3\text{W}_2\text{O}_{12}$ and $\text{La}_{2/3-x}\text{Li}_{3x}\text{TiO}_3$. In $\text{La}_{2/3-x}\text{Li}_{3x}\text{TiO}_3$, Li is always coordinated to the four oxide ions that define the window, as it occupies either the square planar site at the center of the windows (in $\text{La}_{0.62}\text{Li}_{0.16}\text{TiO}_3$ and $\text{La}_{0.5}\text{Li}_{0.5}\text{TiO}_3$ ^{57,88}) or is subject to a small displacement from this site along the $[100]_p$ direction (in $\text{La}_{0.567}\text{Li}_{0.3}\text{TiO}_3$ ^{52,87}), because the near-regular geometry of these sites (small rhombic distortion and regular edge length, producing two diagonals of approximately 4 Å) means that four favorable Li–O distances (of approximately 2 Å) can be obtained simultaneously by occupying them (Figure 11c–f). The center of the O_{12} cage corresponds to an energy maximum for Li in the LLTO family because it would be considerably under-bonded there. In contrast, these sites are not occupied in $\text{La}_3\text{Li}_3\text{W}_2\text{O}_{12}$, where the highly distorted windows have diagonals of 3.3 and 4.6 Å (Figure 11g,h). This precludes the coordination of Li by four oxides from a single window, which would either generate two unphysically short Li–O distances (in the case where Li lies in the plane of the window) or two unphysically long Li–O distances (in the case where Li is displaced from the window along $[100]_p$). Instead, 4-fold coordination of Li is achieved by occupying a distorted tetrahedral site, which is defined by the short diagonals of two adjacent windows, with Li displaced from the centroid of the O_{12} cage along $[110]_p$ (Figure 11g). This site has no equivalent in the $\text{La}_{2/3-x}\text{Li}_{3x}\text{TiO}_3$ structures (Figure 11h), as it is a product of the $b^-b^-c^+$ octahedral tilting. Octahedral tilting and the distortion enforced on the window sites by the B-site alternation between Li and W prevents Li from occupying the sites in the window between the cages, and an appropriate alternative coordination for Li is found within the cage. The resulting A-site Li–O distances lie in the range 2.11(2)–2.20(2) Å with tetrahedral angles in the range 78.4(3)°–131.4(6)° at 5 K.

The site percolation threshold for a simple cubic lattice is 0.31. For an A-site sublattice containing randomly placed 0.25 Li^+ ions, we would therefore not expect a percolating pathway of Li^+ ions throughout the structure, thus limiting the ionic conductivity of such a system, because transport of Li^+ ions through an A-site occupied by an La^{3+} ion is likely to be difficult. Conductivity is strongly suppressed below the site percolation threshold in LLTO and related materials,⁹³ and this combination of A-site blocking by La^{3+} and the absence of Li vacancies in the nominal composition (vacancies are possible within experimental uncertainty) explain the lower NMR and impedance conductivities measured for $\text{La}_3\text{Li}_3\text{W}_2\text{O}_{12}$ than the LLTO family: for example, motional narrowing of the Li NMR occurs at a higher temperature than that observed for $\text{La}_{2/3-x}\text{Li}_{3x}\text{TiO}_3$ (~ 170 K for $x = 0.06$)^{94,95} and doped $\text{Li}_7\text{La}_3\text{Zr}_2\text{O}_{12}$ (< 170 K).⁶⁶ Local ordering of the Li^+ ions, as observed computationally in section 3.3.2, could overcome the percolation problem to some extent by removing some of the randomness that underpins the threshold calculation, forming layers within $\text{La}_3\text{Li}_3\text{W}_2\text{O}_{12}$ with a higher concentration of Li^+ ions. The presence of Li^+ ions on the perovskite B-site opens another pathway to overcome this barrier to long-range diffusion, as long as site exchange between the A- and B-sites is possible. AIMD calculations (section 3.3.4) suggest that this is indeed the case in $\text{La}_3\text{Li}_3\text{W}_2\text{O}_{12}$.

The computed energy landscape for Li^+ ions within $\text{La}_3\text{Li}_3\text{W}_2\text{O}_{12}$ is considerably more complicated than that of $\text{La}_{2/3-x}\text{Li}_{3x}\text{TiO}_3$.⁹⁶ There are multiple local energy minima for

A-site Li^+ ions in $\text{La}_3\text{Li}_3\text{W}_2\text{O}_{12}$ (Figure 4), resulting in an O_{12} cage to O_{12} cage pathway involving multiple events, each with different barriers (Figure 6). Li^+ ions in $\text{La}_{2/3-x}\text{Li}_{3x}\text{TiO}_3$ are proposed to move via single hops of around 4 Å from one window site to the next,⁹⁶ whereas in $\text{La}_3\text{Li}_3\text{W}_2\text{O}_{12}$ single hops take place on the 1.5–2.5 Å length scale (Figure 6), with an energy maximum rather than an energy minimum at the window site. It is likely that Li^+ ion transport in $\text{La}_3\text{Li}_3\text{W}_2\text{O}_{12}$ is best described by a large number of small hopping events with energy barriers of 0.1–0.25 eV, each with differing energy barriers, some of which involve Li^+ ion motion within an O_{12} cage, and others O_{12} cage to neighboring O_{12} cage motion: this 3D diffusion is verified experimentally with the measurements of frequency independent relaxation rates. This mechanism of transport is more closely related to those proposed for the Li^+ ion conducting $\text{Li}_7\text{La}_3\text{Zr}_2\text{O}_{12}$ based garnets⁹⁷ and the $\text{LiTi}_2(\text{PO}_4)_3$ based NASICON systems⁹⁸ than the proposed transport pathways in the perovskite $\text{La}_{2/3-x}\text{Li}_{3x}\text{TiO}_3$, to which $\text{La}_3\text{Li}_3\text{W}_2\text{O}_{12}$ appears more closely related structurally. The different pathways in the two perovskites can be traced to the influence of the distortion of the originally square windows by the B-site Li in $\text{La}_3\text{Li}_3\text{W}_2\text{O}_{12}$ that displaces A-site Li nearer to the cage center and drives octahedral tilting to form the tetrahedral coordination.

DFT barriers between the possible Li^+ ion locations within a single O_{12} cage are less than 0.1 eV (section 3.3.1), and AIMD calculations (Figure 4) suggest that hopping between the sites available to Li within a single O_{12} cage occurs with frequencies of 10^{11} – 10^{12} Hz at room temperature. This is faster than the frequencies probed by NMR line narrowing (10^3 Hz) and relaxometry experiments (10^9 Hz), and AC impedance spectroscopy (10^7 Hz), suggesting that these experiments instead probe rarer hopping events between O_{12} cages which occur at a lower frequency. The computed barriers of 0.11–0.14 eV for single hopping events involving Li passing through the window between two O_{12} cages (labeled 1 and 5 in Figures 6 and S7), are in good agreement to the activation energies of 0.09–0.19 ± 0.02 eV extracted from the low temperature flanks of NMR spin–lattice relaxation rates T_1^{-1} and $T_{1\rho}^{-1}$ data, which reflect single hopping events including unsuccessful jumps within $\text{La}_3\text{Li}_3\text{W}_2\text{O}_{12}$.

The activation energy extracted from the high temperature flank of the $T_{1\rho}^{-1}$ relaxation data (0.26 ± 0.10 eV) and from the jump rates obtained the ⁶⁷Li line narrowing experiments and the $T_{1\rho}^{-1}$ maxima (0.29 ± 0.17 eV) are identical within experimental error, and reflect the barrier to the same 3D translational diffusion process. These values are similar to the maximum energy barrier calculated for the O_{12} cage to neighboring O_{12} cage pathway (Figure 6e) and suggest that we probe this diffusive process, which can involve multiple hops because of the multiple minima on the path. The activation energy obtained on the high temperature flank (0.26 eV) of the $T_{1\rho}^{-1}$ data is similar to those of $\text{La}_{2/3-x}\text{Li}_{3x}\text{TiO}_3$ (0.20 eV for $x = 0.11$,⁸ 0.26 eV for $x = 0.08$,⁷⁶ and 0.26 eV for $x = 0.167$)⁷⁷ and doped $\text{Li}_7\text{La}_3\text{Zr}_2\text{O}_{12}$ (0.34 eV)⁶⁶ which suggests that barrier to O_{12} cage to O_{12} cage Li^+ ion diffusion in $\text{La}_3\text{Li}_3\text{W}_2\text{O}_{12}$ probed by NMR is comparable to the best oxide Li^+ ion conductors reported, despite the considerable structural and Li^+ diffusive pathway differences from the LLTO family.^{7–9} In this phase, the relaxometry plot for Li^+ ions in $\text{La}_{2/3-x}\text{Li}_{3x}\text{TiO}_3$ ($x = 0.11$) shows two motional regimes: at low temperatures ($T < 200$ K) a 2D diffusion process is observed, where only the bottlenecks between O_{12} cages on the same La^{3+} poor layers are

large enough to accommodate Li⁺ ion transport in the material, and a 3D diffusion process above 200 K, where thermal agitation opens up the bottleneck between La³⁺ rich and La³⁺ poor layers allowing Li⁺ to hop between the two layers.^{7–9}

The prefactor τ_0^{-1} in the Arrhenius fit is lower than seen in La_{2/3-x}Li_{3x}TiO₃ ($x = 0.08$, $\tau_0^{-1} = 4.6 \times 10^{11} \text{ s}^{-1}$),⁷⁶ and some other fast Li conductors^{99–101} but comparable to Li₂Ti₃O₇ ($\tau_0^{-1} = 2.5 \times 10^8 \text{ s}^{-1}$).¹⁰² It is below single phonon frequencies in the material and more consistent with a small, temperature-independent contribution to the success of an individual hop, as might arise from a low defect concentration of charge carrying Li vacancy defects, than a single attempt frequency.

The activation energy for Li⁺ site-to-site motion obtained from NMR conductivity ($0.29 \pm 0.17 \text{ eV}$) is smaller than the value determined through impedance measurements ($0.50 \pm 0.05 \text{ eV}$), such a discrepancy is not uncommon in the literature of fast ion conductors,^{69,99,103–105} including La_{2/3-x}Li_{3x}TiO₃,^{76,106} and has been discussed extensively before.¹⁰⁷ The activation energy obtained from the ^{6,7}Li NMR data set can be assigned to migration between O₁₂ cages, whereas that obtained from conductivity is often larger as it may contain additional contributions such as defect formation, and defect association that are involved in longer-range transport of Li between multiple cages: the barriers posed to this by percolation and the low formal vacancy concentration in La₃Li₃W₂O₁₂ are discussed above. Defect creation energies are in the range 0.4–0.6 eV in La₃Li₃W₂O₁₂ from the small supercell calculations presented here. The NMR conductivity is higher than the bulk impedance conductivity by up to 2 orders of magnitude at low temperature (Figure 10b). This discrepancy is observed in other systems,^{69,76,101,107,108} as unsuccessful Li⁺ ion jumps (that is a moving ion returning to its original site rather than hopping further to the next site) contribute to the motional narrowing of the NMR spectra and the relaxation rates without producing longer range Li⁺ ion transport probed by impedance spectroscopy.^{107,109} For example, NMR conductivity is 1 order of magnitude higher than values obtained in impedance spectroscopy for La_{2/3-x}Li_{3x}TiO₃ ($x = 0.08$)⁷⁶ and Li₂ZrO₃.¹⁰⁸

5. CONCLUSIONS

The presence of Li on both the A- and B-sites in La₃Li₃W₂O₁₂ gives it quite different crystal chemistry and Li dynamics from the well-known La_{2/3-x}Li_{3x}TiO₃ family that is based on the same perovskite structure. Although La₃Li₃W₂O₁₂ contains few vacancies and has a blocked percolation path, the barrier to cage-to-cage mobility of the A-site Li is comparable to those in the best known Li conducting oxides. The pathway between cages is more complex in La₃Li₃W₂O₁₂ than in La_{2/3-x}Li_{3x}TiO₃, with multiple minima, because of the quite different A-site Li position which is toward the center of the O₁₂ cage rather than in its windows. This A-site location is produced by the window distortions that are driven by the difference in size between the Li and W cations occupying the B-site and the tilting required to coordinate the A-site Li. A-site to B-site hops are also now possible, and observed in AIMD simulations of Li motion. Control of the defect chemistry in La₃Li₃W₂O₁₂ to increase the carrier concentration and control the A-site to A-site and A-site to B-site pathways thus offers a new route to Li conducting oxides.

■ ASSOCIATED CONTENT

Supporting Information

The Supporting Information is available free of charge on the ACS Publications website at DOI: 10.1021/acs.chemmater.6b03220.

TEM-EDX and ICP-OES data, additional diffraction data and refinement table, local A-site Li coordination environments of DFT calculated structures, additional ⁶Li MAS NMR spectra, La₃Li₃W₂O₁₂ temperature stability test and dilatometry plot (PDF)

■ AUTHOR INFORMATION

Corresponding Authors

*E-mail: frederic.blanc@liverpool.ac.uk (F.B.).

*E-mail: m.j.rosseinsky@liverpool.ac.uk (M.J.R.).

Notes

The authors declare no competing financial interest.

■ ACKNOWLEDGMENTS

We thank George Miller for ICP-OES measurements, Dr. Claire Murray and Prof. Chiu Tang for assistance on beamline I11 (Diamond, UK), Dr. Kevin Knight and Dr. Dominic Fortes for assistance on HRPD (ISIS, UK) and Dr. Pierre Florian (CEMHTI-CNRS, France) for access to the laser-heated high-temperature static NMR probe and fruitful discussions. We thank EPSRC for funding under EP/H000925 and EP/N004884 and a studentship to K.K.I. F.B. thanks the University of Liverpool and the STFC for funding via an Early Career Award. Computational resources were provided by the University of Liverpool, the N8 HPC Centre of Excellence, provided and funded by the N8 consortium and EPSRC (EP/K000225/1), and the ARCHER UK National Supercomputing Service (<http://www.archer.ac.uk>) via our membership of the UK's HEC Materials Chemistry Consortium, which is funded by EPSRC (EP/L000202). The UK 850 MHz solid-state NMR Facility used in this research was funded by EPSRC and BBSRC (contract reference PR140003), as well as the University of Warwick including via part funding through Birmingham Science City Advanced Materials Projects 1 and 2 supported by Advantage West Midlands (AWM) and the European Regional Development Fund (ERDF). Collaborative assistance from the 850 MHz Facility Manager (Dr. Dinu Iuga, University of Warwick) is acknowledged. M.J.R. is a Royal Society Research Professor. Original data is also available at the University of Liverpool's DataCat repository at DOI: 10.17638/datacat.liverpool.ac.uk/162. The supporting crystallographic information files may be obtained from FIZ Karlsruhe, 76344 Eggenstein- Leopoldshafen, Germany (e-mail: crysdata@fiz-karlsruhe.de), on quoting the deposition numbers CSD-432008 and CSD-432009.

■ REFERENCES

- (1) Bachman, J. C.; Muy, S.; Grimaud, A.; Chang, H.-H.; Pour, N.; Lux, S. F.; Paschos, O.; Maglia, F.; Lupart, S.; Lamp, P.; Giordano, L.; Shao-Horn, Y. Inorganic Solid-State Electrolytes for Lithium Batteries: Mechanisms and Properties Governing Ion Conduction. *Chem. Rev.* **2016**, *116*, 140–162.
- (2) Kamaya, N.; Homma, K.; Yamakawa, Y.; Hirayama, M.; Kanno, R.; Yonemura, M.; Kamiyama, T.; Kato, Y.; Hama, S.; Kawamoto, K.; Mitsui, A. A Lithium Superionic Conductor. *Nat. Mater.* **2011**, *10*, 682–686.

- (3) Kuhn, A.; Gerbig, O.; Zhu, C.; Falkenberg, F.; Maier, J.; Lotsch, B. V. A New Ultrafast Superionic Li-Conductor: Ion Dynamics in $\text{Li}_{11}\text{Si}_2\text{P}_2\text{S}_{12}$ and Comparison with Other Tetragonal LGPS-Type Electrolytes. *Phys. Chem. Chem. Phys.* **2014**, *16*, 14669–14674.
- (4) Muramatsu, H.; Hayashi, A.; Ohtomo, T.; Hama, S.; Tatsumisago, M. Structural Change of $\text{Li}_2\text{S-P}_2\text{S}_5$ Sulfide Solid Electrolytes in the Atmosphere. *Solid State Ionics* **2011**, *182*, 116–119.
- (5) Aguesse, F.; López del Amo, J. M.; Roddatis, V.; Aguadero, A.; Kilner, J. A. Enhancement of the Grain Boundary Conductivity in Ceramic $\text{Li}_{0.34}\text{La}_{0.55}\text{TiO}_3$ Electrolytes in a Moisture-Free Processing Environment. *Adv. Mater. Interfaces* **2014**, *1*, 910–924.
- (6) Bernuy-Lopez, C.; Manalastas, W.; Lopez Del Amo, J. M.; Aguadero, A.; Aguesse, F.; Kilner, J. A. Atmosphere Controlled Processing of Ga-Substituted Garnets for High Li-Ion Conductivity Ceramics. *Chem. Mater.* **2014**, *26*, 3610–3617.
- (7) Emery, J.; Bohnké, O.; Fourquet, J. L.; Buzaré, J. Y.; Florian, P.; Massiot, D. Nuclear Magnetic Resonance Investigation of Li^+ -Ion Dynamics in the Perovskite Fast-Ion Conductor $\text{Li}_{3-x}\text{La}_{2/3-x}\text{TiO}_3$. *J. Phys.: Condens. Matter* **2002**, *14*, 523–539.
- (8) Bohnke, O.; Emery, J.; Fourquet, J. L. Anomalies in Li^+ Ion Dynamics Observed by Impedance Spectroscopy and ^7Li NMR in the Perovskite Fast Ion Conductor $(\text{Li}_{3-x}\text{La}_{2/3-x}\text{TiO}_3)$. *Solid State Ionics* **2003**, *158*, 119–132.
- (9) Bohnke, O. The Fast Lithium-Ion Conducting Oxides $\text{Li}_{3-x}\text{La}_{2/3-x}\text{TiO}_3$ from Fundamentals to Application. *Solid State Ionics* **2008**, *179*, 9–15.
- (10) Knauth, P. Inorganic Solid Li Ion Conductors: An Overview. *Solid State Ionics* **2009**, *180*, 911–916.
- (11) Belous, A. G.; Gavrilenko, O. N.; Pashkova, E. V.; Danil'chenko, K. P.; Vyunov, O. I. Effect of Synthesis Conditions on the Lithium Nonstoichiometry and Properties of $\text{La}_{2/3-x}\text{Li}_{3x}\text{M}_2\text{O}_6$ ($M = \text{Nb}, \text{Ta}$) Perovskite-like Solid Solutions. *Inorg. Mater.* **2004**, *40*, 867–873.
- (12) Yang, K.-Y.; Fung, K.-Z. Effect of Li^+ Addition on Crystal Structure and Electrical Conduction of Highly Defective $\text{La}_{1/3}\text{NbO}_3$ Perovskite. *J. Phys. Chem. Solids* **2008**, *69*, 393–399.
- (13) Arakawa, S.; Shiotsu, T.; Hayashi, S. Non-Arrhenius Temperature Dependence of Conductivity in Lanthanum Lithium Tantalate. *J. Ceram. Soc. Japan* **2005**, *113*, 317–319.
- (14) Mizumoto, K.; Hayashi, S. Crystal Structure and Lithium Ion Conductivity of A-Site Deficient Perovskites $\text{La}_{1/3-x}\text{Li}_{3x}\text{TaO}_3$. *J. Ceram. Soc. Japan* **1997**, *105*, 713–715.
- (15) Mizumoto, K.; Hayashi, S. Lithium Ion Conduction in A-Site Deficient Perovskites $\text{R}_{1/4}\text{Li}_{1/4}\text{TaO}_3$ ($R = \text{La}, \text{Nd}, \text{Sm}$ and Y). *Solid State Ionics* **1999**, *116*, 263–269.
- (16) Vijayakumar, M.; Emery, J.; Bohnke, O.; Vold, R. L.; Hoatson, G. L. ^7Li NMR Analysis on Perovskite Structured $\text{Li}_{0.15}\text{La}_{0.28}\text{TaO}_3$. *Solid State Ionics* **2006**, *177*, 1673–1676.
- (17) Katsumata, T.; Takahata, M.; Mochizuki, N.; Inaguma, Y. The Relationship between Li Ion Conductivity and Crystal Structure for Ordered Perovskite Compounds, $(\text{La}_{2/3-1/3p}\text{Li}_p)(\text{Mg}_{1/2}\text{W}_{1/2})\text{O}_3$ ($p = 0.05, 0.11$ and 0.14). *Solid State Ionics* **2004**, *171*, 191–198.
- (18) Chung, H.-T.; Kim, J.-G.; Kim, H.-G. Dependence of the Lithium Ionic Conductivity on the B-Site Ion Substitution in $(\text{Li}_{0.5}\text{La}_{0.5})\text{Ti}_{1-x}\text{M}_x\text{O}_3$ ($M = \text{Sn}, \text{Zr}, \text{Mn}, \text{Ge}$). *Solid State Ionics* **1998**, *107*, 153–160.
- (19) Harada, Y.; Watanabe, H.; Kuwano, J.; Saito, Y. Lithium Ion Conductivity of A-Site Deficient Perovskite Solid Solutions. *J. Power Sources* **1999**, *81*–82, 777–781.
- (20) Thangadurai, V.; Shukla, A. K.; Gopalakrishnan, J. $\text{LiSr}_{1.65}\text{B}_{1.3}\text{B}'_{1.7}\text{O}_9$ ($B = \text{Ti}, \text{Zr}; B' = \text{Nb}, \text{Ta}$): New Lithium Ion Conductors Based on the Perovskite Structure. *Chem. Mater.* **1999**, *11*, 835–839.
- (21) Sebastian, L.; Gopalakrishnan, J. Lithium Ion Mobility in Metal Oxides: A Materials Chemistry Perspective. *J. Mater. Chem.* **2003**, *13*, 433–441.
- (22) Borisevich, A. Y.; Davies, P. K. $\text{La}(\text{Li}_{1/3}\text{Ti}_{2/3})\text{O}_3$: A New 1:2 Ordered Perovskite. *J. Solid State Chem.* **2003**, *170*, 198–201.
- (23) Kirk, C. A.; West, A. R. Crystal Structure of the Perovskite-Related Phase of Approximate Composition $\text{LaLi}_{1/3}\text{Ti}_{2/3}\text{O}_3$. *Solid State Sci.* **2002**, *4*, 1163–1166.
- (24) Hikichi, Y.; Suzuki, S. Preparation of Cubic Perovskites $\text{A}(\text{B}_{2/5}\text{W}_{3/5})\text{O}_3$ ($A = \text{Ba}$ or Sr , $B = \text{Na}$ or Li). *J. Am. Ceram. Soc.* **1987**, *70*, C-99–C-100.
- (25) Demazeau, G.; Oh-Kim, E.; Choy, J.; Hagenmuller, P. A Vanadate (V) Oxide with Perovskite Structure: La_2LiVO_6 , Comparison with Homologous La_2LiMO_6 Phases ($M = \text{Fe}, \text{Nb}, \text{Mo}, \text{Ru}, \text{Ta}, \text{Re}, \text{Os}, \text{Ir}$). *Mater. Res. Bull.* **1987**, *22*, 735–740.
- (26) Hayashi, K.; Noguchi, H.; Ishii, M. Preparation and Vibrational Spectra of La_2LiMO_6 ($M = \text{Nb}, \text{Ta}, \text{Mo}, \text{Re}, \text{Ru}, \text{Os},$ and Ir). *Mater. Res. Bull.* **1986**, *21*, 401–406.
- (27) López, M. L.; Veiga, M. L.; Rodríguez-Carvajal, J.; Fernández, F.; Jerez, A.; Pico, C. The Monoclinic Perovskite $\text{La}_2\text{LiSbO}_6$. A Rietveld Refinement of Neutron Powder Diffraction Data. *Mater. Res. Bull.* **1992**, *27*, 647–654.
- (28) Wu, H.; Davies, P. K. Non-Stoichiometric 1:2 Ordered Perovskites in the $\text{Ba}(\text{Li}_{1/4}\text{Nb}_{3/4})\text{O}_3$ - $\text{Ba}(\text{Li}_{2/5}\text{W}_{3/5})\text{O}_3$ System. *J. Solid State Chem.* **2004**, *177*, 3469–3478.
- (29) Wu, H.; Davies, P. K. Ordered Perovskites in the $\text{A}^{2+}(\text{Li}_{1/4}\text{Nb}_{3/4})\text{O}_3$ - $\text{A}^{2+}(\text{Li}_{2/5}\text{W}_{3/5})\text{O}_3$ ($\text{A}^{2+} = \text{Sr}, \text{Ca}$) Systems. *J. Solid State Chem.* **2004**, *177*, 4305–4315.
- (30) MacKenzie, K. J. D.; Smith, M. E. *Multinuclear Solid-State Nuclear Magnetic Resonance of Inorganic Materials*; Elsevier: Oxford, 2002.
- (31) Ashbrook, S. E.; Smith, M. E. Solid State ^{17}O NMR—an Introduction to the Background Principles and Applications to Inorganic Materials. *Chem. Soc. Rev.* **2006**, *35*, 718–735.
- (32) Coelho, A. A. *Topas Academic*, Version 5; Coelho Software: Brisbane, Australia, 2012.
- (33) Larson, A. C.; Von Dreele, R. B. *General Structure Analysis System (GSAS)*; Los Alamos National Laboratory: Los Alamos, NM, 1994.
- (34) Toby, B. H. EXPGUI, a Graphical User Interface for GSAS. *J. Appl. Crystallogr.* **2001**, *34*, 210–213.
- (35) Perdew, J. P.; Burke, K.; Ernzerhof, M. Generalized Gradient Approximation Made Simple. *Phys. Rev. Lett.* **1996**, *77*, 3865–3868.
- (36) Kresse, G.; Furthmüller, J. Efficient Iterative Schemes for *Ab Initio* Total-Energy Calculations Using a Plane-Wave Basis Set. *Phys. Rev. B: Condens. Matter Mater. Phys.* **1996**, *54*, 11169–11186.
- (37) Kresse, G.; Joubert, D. From Ultrasoft Pseudopotentials to the Projector Augmented-Wave Method. *Phys. Rev. B: Condens. Matter Mater. Phys.* **1999**, *59*, 1758–1775.
- (38) Pickard, C. J.; Mauri, F. All-Electron Magnetic Response with Pseudopotentials: NMR Chemical Shifts. *Phys. Rev. B: Condens. Matter Mater. Phys.* **2001**, *63*, 245101.
- (39) Yates, J. R.; Pickard, C. J.; Mauri, F. Calculation of NMR Chemical Shifts for Extended Systems Using Ultrasoft Pseudopotentials. *Phys. Rev. B: Condens. Matter Mater. Phys.* **2007**, *76*, 024401.
- (40) Clark, S. J.; Segall, M. D.; Pickard, C. J.; Hasnip, P. J.; Probert, M. I. J.; Refson, K.; Payne, M. C. First Principles Methods Using CASTEP. *Z. Kristallogr. - Cryst. Mater.* **2005**, *220*, 567–570.
- (41) Middlemiss, D. S.; Blanc, F.; Pickard, C. J.; Grey, C. P. Solid-State NMR Calculations for Metal Oxides and Gallates: Shielding and Quadrupolar Parameters for Perovskites and Related Phases. *J. Magn. Reson.* **2010**, *204*, 1–10.
- (42) Frydman, L.; Harwood, J. S. Isotropic Spectra of Half-Integer Quadrupolar Spins from Bidimensional Magic-Angle Spinning NMR. *J. Am. Chem. Soc.* **1995**, *117*, 5367–5368.
- (43) Medek, A.; Harwood, J. S.; Frydman, L. Multiple-Quantum Magic-Angle Spinning NMR: A New Method for the Study of Quadrupolar Nuclei in Solids. *J. Am. Chem. Soc.* **1995**, *117*, 12779–12787.
- (44) Amoureux, J.-P.; Fernandez, C.; Steuernagel, S. Z Filtering in MQMAS NMR. *J. Magn. Reson., Ser. A* **1996**, *123*, 116–118.
- (45) Lacassagne, V.; Bessada, C.; Florian, P.; Bouvet, S.; Ollivier, B.; Coutures, J.-P.; Massiot, D. Structure of High-Temperature NaF —

AlF₃–Al₂O₃ Melts: A Multinuclear NMR Study. *J. Phys. Chem. B* **2002**, *106*, 1862–1868.

(46) Lacassagne, V.; Bessada, C.; Ollivier, B.; Massiot, D.; Florian, P.; Coutures, J.-P. Étude de la Transition Solide/Liquide de la Cryolithe par Résonance Magnétique Nucléaire de ²⁷Al, ²³Na et ¹⁹F. *C. R. Acad. Sci., Ser. IIB: Mec., Phys., Chim., Astron.* **1997**, *325*, 91–98.

(47) Bielecki, A.; Burum, D. P. Temperature Dependence of ²⁰⁷Pb MAS Spectra of Solid Lead Nitrate. An Accurate, Sensitive Thermometer for Variable-Temperature MAS. *J. Magn. Reson., Ser. A* **1995**, *116*, 215–220.

(48) Beckmann, P. A.; Dybowski, C. A Thermometer for Nonspinning Solid-State NMR Spectroscopy. *J. Magn. Reson.* **2000**, *146*, 379–380.

(49) Becker, K. D. Temperature Dependence of NMR Chemical Shifts in Cuprous Halides. *J. Chem. Phys.* **1978**, *68*, 3785–3793.

(50) Wu, J.; Kim, N.; Stebbins, J. F. Temperature Calibration for High-Temperature MAS NMR to 913 K: ⁶³Cu MAS NMR of CuBr and CuI, and ²³Na MAS NMR of NaNbO₃. *Solid State Nucl. Magn. Reson.* **2011**, *40*, 45–50.

(51) Woodward, P. M. Octahedral Tilting in Perovskites. I. Geometrical Considerations. *Acta Crystallogr., Sect. B: Struct. Sci.* **1997**, *53*, 32–43.

(52) Sommariva, M.; Catti, M. Neutron Diffraction Study of Quenched Li_{0.3}La_{0.567}TiO₃ Lithium Ion Conducting Perovskite. *Chem. Mater.* **2006**, *18*, 2411–2417.

(53) García-Martín, S.; Alario-Franco, M. A.; Ehrenberg, H.; Rodríguez-Carvajal, J.; Amador, U. Crystal Structure and Microstructure of Some La_{2/3-x}Li_{3x}TiO₃ Oxides: An Example of the Complementary Use of Electron Diffraction and Microscopy and Synchrotron X-Ray Diffraction To Study Complex Materials. *J. Am. Chem. Soc.* **2004**, *126*, 3587–3596.

(54) Ibarra, J.; Várez, A.; León, C.; Santamaría, J.; Torres-Martínez, L. M.; Sanz, J. Influence of Composition on the Structure and Conductivity of the Fast Ionic Conductors La_{2/3-x}Li_{3x}TiO₃ (0.03 ≤ x ≤ 0.167). *Solid State Ionics* **2000**, *134*, 219–228.

(55) Kennedy, B. J.; Howard, C. J.; Kubota, Y.; Kato, K. Phase Transition Behaviour in the A-Site Deficient Perovskite Oxide La_{1/3}NbO₃. *J. Solid State Chem.* **2004**, *177*, 4552–4556.

(56) Khalyavin, D. D.; Senos, A. M. R.; Mantas, P. Q. Crystal Structure of La₄Mg₃W₃O₁₈ Layered Oxide. *J. Phys.: Condens. Matter* **2005**, *17*, 2585–2595.

(57) Yashima, M.; Itoh, M.; Inaguma, Y.; Morii, Y. Crystal Structure and Diffusion Path in the Fast Lithium-Ion Conductor La_{0.62}Li_{0.16}TiO₃. *J. Am. Chem. Soc.* **2005**, *127*, 3491–3495.

(58) Fourquet, J. L.; Duroy, H.; Crosnier-Lopez, M. P. Structural and Microstructural Studies of the Series La_{2/3-x}Li_{3x}□_{1/3-2x}TiO₃. *J. Solid State Chem.* **1996**, *127*, 283–294.

(59) Khalyavin, D. D.; Senos, A. M. R.; Mantas, P. Q.; Argyriou, D. N.; Gomes, I. T.; Vieira, L. G.; Ribeiro, J. L. Structure and Dielectric Characterization of a New A-Site Deficient La_{5/3}MgTaO₆ Perovskite. *J. Solid State Chem.* **2007**, *180*, 41–48.

(60) Grau-Crespo, R.; Hamad, S.; Catlow, C. R. A.; de Leeuw, N. H. Symmetry-Adapted Configurational Modelling of Fractional Site Occupancy in Solids. *J. Phys.: Condens. Matter* **2007**, *19*, 256201.

(61) Khalyavin, D. D.; Lopes, A. B.; Senos, A. M. R.; Mantas, P. Q. Crystal Structure of La₆Mg₄Ta₂W₂O₂₄ Oxide: A Representative of a Novel A_{3n}B'_{2n}B''_{2n}O_{12n} Homologous Series with n = 2. *Chem. Mater.* **2006**, *18*, 3843–3849.

(62) Xu, Z.; Stebbins, J. F. Cation Dynamics and Diffusion in Lithium Orthosilicate: Two-Dimensional Lithium-6 NMR. *Science* **1995**, *270*, 1332–1334.

(63) Xu, Z.; Stebbins, J. F. ⁶Li Nuclear Magnetic Resonance Chemical Shifts, Coordination Number and Relaxation in Crystalline and Glassy Silicates. *Solid State Nucl. Magn. Reson.* **1995**, *5*, 103–112.

(64) Wilkening, M.; Küchler, W.; Heitjans, P. From Ultraslow to Fast Lithium Diffusion in the 2D Ion Conductor Li_{0.7}TiS₂ Probed Directly by Stimulated-Echo NMR and Nuclear Magnetic Relaxation. *Phys. Rev. Lett.* **2006**, *97*, 065901.

(65) Kuhn, A.; Sreeraj, P.; Pöttgen, R.; Wiemhöfer, H.-D.; Wilkening, M.; Heitjans, P. Li Ion Diffusion in the Anode Material Li₁₂Si₇: Ultrafast Quasi-1D Diffusion and Two Distinct Fast 3D Jump Processes Separately Revealed by ⁷Li NMR Relaxometry. *J. Am. Chem. Soc.* **2011**, *133*, 11018–11021.

(66) Buschmann, H.; Dölle, J.; Berendts, S.; Kuhn, A.; Bottke, P.; Wilkening, M.; Heitjans, P.; Senyshyn, A.; Ehrenberg, H.; Lotnyk, A.; Duppel, V.; Kienle, L.; Janek, J. Structure and Dynamics of the Fast Lithium Ion Conductor “Li₇La₃Zr₂O₁₂”. *Phys. Chem. Chem. Phys.* **2011**, *13*, 19378–19392.

(67) Blanc, F.; Middlemiss, D. S.; Gan, Z.; Grey, C. P. Defects in Doped LaGaO₃ Anionic Conductors: Linking NMR Spectral Features, Local Environments, and Defect Thermodynamics. *J. Am. Chem. Soc.* **2011**, *133*, 17662–17672.

(68) Epp, V.; Gün, Ö.; Deiseroth, H.-J.; Wilkening, M. Long-Range Li⁺ Dynamics in the Lithium Argyrodite Li₇PSe₆ as Probed by Rotating-Frame Spin-Lattice Relaxation NMR. *Phys. Chem. Chem. Phys.* **2013**, *15*, 7123–7132.

(69) Enciso-Maldonado, L.; Dyer, M. S.; Jones, M. D.; Li, M.; Payne, J. L.; Pitcher, M. J.; Omir, M. K.; Claridge, J. B.; Blanc, F.; Rosseinsky, M. J. Computational Identification and Experimental Realization of Lithium Vacancy Introduction into the Olivine LiMgPO₄. *Chem. Mater.* **2015**, *27*, 2074–2091.

(70) Liu, T.; Leskes, M.; Yu, W.; Moore, A. J.; Zhou, L.; Bayley, P. M.; Kim, G.; Grey, C. P. Cycling Li-O₂ Batteries via LiOH Formation and Decomposition. *Science* **2015**, *350*, 530–533.

(71) Bonhomme, C.; Gervais, C.; Babonneau, F.; Coelho, C.; Pourpoint, F.; Azaïs, T.; Ashbrook, S. E.; Griffin, J. M.; Yates, J. R.; Mauri, F.; Pickard, C. J. First-Principles Calculation of NMR Parameters Using the Gauge Including Projector Augmented Wave Method: A Chemist's Point of View. *Chem. Rev.* **2012**, *112*, 5733–5779.

(72) Smith, M. E.; van Eck, E. R. H. Recent Advances in Experimental Solid State NMR Methodology for Half-Integer Spin Quadrupolar Nuclei. *Prog. Nucl. Magn. Reson. Spectrosc.* **1999**, *34*, 159–201.

(73) Ashbrook, S. E.; Dawson, D. M. Exploiting Periodic First-Principles Calculations in NMR Spectroscopy of Disordered Solids. *Acc. Chem. Res.* **2013**, *46*, 1964–1974.

(74) Shannon, R. D. Revised Effective Ionic Radii and Systematic Studies of Interatomic Distances in Halides and Chalcogenides. *Acta Crystallogr., Sect. A: Cryst. Phys., Diffr., Theor. Gen. Crystallogr.* **1976**, *32*, 751–767.

(75) Böhmer, R.; Jeffrey, K. R.; Vogel, M. Solid-State Li NMR with Applications to the Translational Dynamics in Ion Conductors. *Prog. Nucl. Magn. Reson. Spectrosc.* **2007**, *50*, 87–174.

(76) Emery, J.; Buzare, J. Y.; Bohnke, O.; Fourquet, J. L. Lithium-7 NMR and Ionic Conductivity Studies of Lanthanum Lithium Titanate Electrolytes. *Solid State Ionics* **1997**, *99*, 41–51.

(77) Bucheli, W.; Arbi, K.; Sanz, J.; Nuzhnyy, D.; Kamba, S.; Várez, A.; Jimenez, R. Near Constant Loss Regime in Fast Ionic Conductors Analyzed by Impedance and NMR Spectroscopies. *Phys. Chem. Chem. Phys.* **2014**, *16*, 15346–15354.

(78) Abragam, A. *The Principles of Nuclear Magnetism*; Oxford University Press: Oxford, 1961.

(79) Heitjans, P.; Schirmer, A.; Indris, S. *NMR and β-NMR Studies of Diffusion in Interface-Dominated and Disordered Solids*; Heitjans, P., Kärger, J., Eds.; Springer-Verlag: Berlin, 2005.

(80) Wilkening, M.; Heitjans, P. From Micro to Macro: Access to Long-Range Li⁺ Diffusion Parameters in Solids via Microscopic ^{6,7}Li Spin-Alignment Echo NMR Spectroscopy. *ChemPhysChem* **2012**, *13*, 53–65.

(81) Bloembergen, N.; Purcell, E. M.; Pound, R. V. Relaxation Effects in Nuclear Magnetic Resonance Absorption. *Phys. Rev.* **1948**, *73*, 679–712.

(82) Irvine, J. T. S.; Sinclair, D. C.; West, A. R. Electroceramics: Characterization by Impedance Spectroscopy. *Adv. Mater.* **1990**, *2*, 132–138.

- (83) Stramare, S.; Thangadurai, V.; Weppner, W. Lithium Lanthanum Titanates: A Review. *Chem. Mater.* **2003**, *15*, 3974–3990.
- (84) García-Martín, S.; Amador, U.; Morata-Orrantía, A.; Rodríguez-Carvajal, J.; Alario-Franco, M. Á. Structure, Microstructure, Composition and Properties of Lanthanum Lithium Titanates and Some Substituted Analogues. *Z. Anorg. Allg. Chem.* **2009**, *635*, 2363–2373.
- (85) Marezio, M.; Remeika, J. P.; Dernier, P. D. The Crystal Chemistry of the Rare Earth Orthoferrites. *Acta Crystallogr., Sect. B: Struct. Crystallogr. Cryst. Chem.* **1970**, *26*, 2008–2022.
- (86) López, M. L.; Veiga, M. L.; Jerez, A.; Pico, C. Synthesis and Crystal Structure of $\text{La}_2\text{LiSbO}_6$. *Mater. Res. Bull.* **1990**, *25*, 1271–1277.
- (87) Catti, M.; Sommariva, M.; Ibberson, R. M. Tetragonal Superstructure and Thermal History of $\text{Li}_{0.3}\text{La}_{0.567}\text{TiO}_3$ (LLTO) Solid Electrolyte by Neutron Diffraction. *J. Mater. Chem.* **2007**, *17*, 1300–1307.
- (88) Alonso, J. A.; Sanz, J.; Santamaría, J.; León, C.; Várez, A.; Fernández-Díaz, M. T. On the Location of Li^+ Cations in the Fast Li-Cation Conductor $\text{La}_{0.5}\text{Li}_{0.5}\text{TiO}_3$ Perovskite. *Angew. Chem. Int. Ed.* **2000**, *39*, 619–621.
- (89) Momma, K.; Izumi, F. VESTA 3 for Three-Dimensional Visualization of Crystal, Volumetric and Morphology Data. *J. Appl. Crystallogr.* **2011**, *44*, 1272–1276.
- (90) Baur, W. H. The Geometry of Polyhedral Distortions. Predictive Relationships for the Phosphate Group. *Acta Crystallogr., Sect. B: Struct. Crystallogr. Cryst. Chem.* **1974**, *30*, 1195–1215.
- (91) Robinson, K.; Gibbs, G. V.; Ribbe, P. H. Quadratic Elongation: A Quantitative Measure of Distortion in Coordination Polyhedra. *Science* **1971**, *172*, 567–570.
- (92) Buttner, R. H.; Maslen, E. N. Electron Difference Density and Structural Parameters in CaTiO_3 . *Acta Crystallogr., Sect. B: Struct. Sci.* **1992**, *48*, 644–649.
- (93) Inaguma, Y. Fast Percolative Diffusion in Lithium Ion-Conducting Perovskite-Type Oxides. *J. Ceram. Soc. Japan* **2006**, *114*, 1103–1110.
- (94) Rivera, A.; Sanz, J. Lithium Dynamics in the Fast Ionic Conductor $\text{Li}_{0.18}\text{La}_{0.61}\text{TiO}_3$ Probed by ^7Li NMR Spectroscopy. *Phys. Rev. B: Condens. Matter Mater. Phys.* **2004**, *70*, 094301.
- (95) Rivera, A.; León, C.; Santamaría, J.; Várez, A.; Paris, M. A.; Sanz, J. $\text{Li}_{3x}\text{La}_{2(2/3-x)}\text{TiO}_3$ Fast Ionic Conductors. Correlation between Lithium Mobility and Structure. *J. Non-Cryst. Solids* **2002**, *307–310*, 992–998.
- (96) Catti, M. Short-Range Order and Li^+ Ion Diffusion Mechanisms in $\text{Li}_3\text{La}_6\text{□}_2(\text{TiO}_3)_{16}$ (LLTO). *Solid State Ionics* **2011**, *183*, 1–6.
- (97) Jalem, R.; Yamamoto, Y.; Shiiba, H.; Nakayama, M.; Munakata, H.; Kasuga, T.; Kanamura, K. Concerted Migration Mechanism in the Li Ion Dynamics of Garnet-Type $\text{Li}_7\text{La}_3\text{Zr}_2\text{O}_{12}$. *Chem. Mater.* **2013**, *25*, 425–430.
- (98) Lang, B.; Ziebarth, B.; Elsässer, C. Lithium Ion Conduction in $\text{LiTi}_2(\text{PO}_4)_3$ and Related Compounds Based on the NASICON Structure: A First-Principles Study. *Chem. Mater.* **2015**, *27*, 5040–5048.
- (99) Kuhn, A.; Duppel, V.; Lotsch, B. V. Tetragonal $\text{Li}_{10}\text{GeP}_2\text{S}_{12}$ and Li_7GePS_8 – Exploring the Li Ion Dynamics in LGPS Li Electrolytes. *Energy Environ. Sci.* **2013**, *6*, 3548–3552.
- (100) Epp, V.; Gün, Ö.; Deiseroth, H.-J.; Wilkening, M. Highly Mobile Ions: Low Temperature NMR Directly Probes Extremely Fast Li^+ Hopping in Argyrodite-Type $\text{Li}_6\text{PS}_3\text{Br}$. *J. Phys. Chem. Lett.* **2013**, *4*, 2118–2123.
- (101) Epp, V.; Ma, Q.; Hammer, E.-V.; Tietz, F.; Wilkening, M. Very Fast Bulk Li Ion Diffusivity in Crystalline $\text{Li}_{1.5}\text{Al}_{0.5}\text{Ti}_{1.5}(\text{PO}_4)_3$ as Seen by NMR Relaxometry. *Phys. Chem. Chem. Phys.* **2015**, *17*, 32115–32121.
- (102) Huberman, B. A.; Boyce, J. B. Breakdown of Absolute Rate Theory and Prefactor Anomalies in Superionic Conductors. *Solid State Commun.* **1978**, *25*, 843–846.
- (103) Latie, L.; Villeneuve, G.; Conte, D.; Le Flem, G. Ionic Conductivity of Oxides with General Formula $\text{Li}_x\text{Ln}_{1/3}\text{Nb}_{1-x}\text{Ti}_x\text{O}_3$ ($\text{Ln} = \text{La}, \text{Nd}$). *J. Solid State Chem.* **1984**, *51*, 293–299.
- (104) Deng, Y.; Eames, C.; Chotard, J.-N.; Lalère, F.; Seznec, V.; Emge, S.; Pecher, O.; Grey, C. P.; Masquelier, C.; Islam, M. S. Structural and Mechanistic Insights into Fast Lithium-Ion Conduction in $\text{Li}_4\text{SiO}_4\text{--Li}_3\text{PO}_4$ Solid Electrolytes. *J. Am. Chem. Soc.* **2015**, *137*, 9136–9145.
- (105) Arbi, K.; Lazarraga, M. G.; Ben Hassen Chehimi, D.; Ayadi-Trabelsi, M.; Rojo, J. M.; Sanz, J. Lithium Mobility in $\text{Li}_{1.2}\text{Ti}_{1.8}\text{R}_{0.2}(\text{PO}_4)_3$ Compounds ($\text{R} = \text{Al}, \text{Ga}, \text{Sc}, \text{In}$) as Followed by NMR and Impedance Spectroscopy. *Chem. Mater.* **2004**, *16*, 255–262.
- (106) León, C.; Lucía, M.; Santamaría, J.; París, M.; Sanz, J.; Várez, A. Electrical Conductivity Relaxation and Nuclear Magnetic Resonance of Li Conducting $\text{Li}_{0.5}\text{La}_{0.5}\text{TiO}_3$. *Phys. Rev. B: Condens. Matter Mater. Phys.* **1996**, *54*, 184–189.
- (107) Kim, N.; Hsieh, C.-H.; Huang, H.; Prinz, F. B.; Stebbins, J. F. High Temperature ^{17}O MAS NMR Study of Calcia, Magnesia, Scandia and Yttria Stabilized Zirconia. *Solid State Ionics* **2007**, *178*, 1499–1506.
- (108) Bottke, P.; Freude, D.; Wilkening, M. Ultraslow Li Exchange Processes in Diamagnetic Li_2ZrO_3 as Monitored by EXSY NMR. *J. Phys. Chem. C* **2013**, *117*, 8114–8119.
- (109) Holmes, L.; Peng, L.; Heinmaa, L.; O'Dell, L. A.; Smith, M. E.; Vannier, R.-N.; Grey, C. P. Variable-Temperature ^{17}O NMR Study of Oxygen Motion in the Anionic Conductor $\text{Bi}_{26}\text{Mo}_{10}\text{O}_{69}$. *Chem. Mater.* **2008**, *20*, 3638–3648.